

Stirring of sea ice meltwater enhances submesoscale fronts in the Southern Ocean

I. Giddy^{1,2,3}, S. Swart^{1,2}, A.F. Thompson⁴, M. du Plessis^{2,3}, S. A. Nicholson³

¹Department of Oceanography, University of Cape Town, Rondebosch, South Africa

²Department of Marine Sciences, University of Gothenburg, Gothenburg, Sweden

³Southern Ocean Carbon-Climate Observatory (SOCCO), CSIR, Cape Town, South Africa

⁴Environmental Science and Engineering, California Institute of Technology, Pasadena, CA, USA

Key Points:

- Sea ice meltwater controls the buoyancy of the mixed layer during early summer
- Mixed layer eddies grow from mesoscale meltwater lateral gradients but are confined to the surface boundary layer
- Observations suggest that mixed layer variability at submesoscales is dominated by wind-front interactions

Corresponding author: Isabelle Giddy, isgiddy@gmail.com

Abstract

In the sea ice-impacted Southern Ocean, the spring melt of sea ice modifies the upper ocean. These modified waters subduct and enter the global overturning circulation. Submesoscale processes act to modulate the stratification of the mixed layer and therefore mixed layer properties. Sparse observations mean that the role of submesoscales in exchange across the base of the mixed layer in this region is not well constrained. The goal of this study is to determine the interplay between sea ice melt, surface boundary layer forcing, and submesoscale flows in regulating the mixed layer structure in the Antarctic Marginal Ice Zone. High-resolution observations suggest that fine-scale lateral fronts, representative of submesoscale mixed layer eddies (MLEs), arise from mesoscale gradients produced by northwards advecting sea ice meltwater. The strong salinity-driven stratification at the base of the mixed layer confined the MLEs to the upper ocean, limiting submesoscale vertical fluxes across the mixed layer base. This strong stratification prevents the local subduction by submesoscale flow of these modified waters, suggesting that the subduction site that links to the global overturning circulation does not correspond with the location of sea ice melt. However, the presence of MLEs enhanced the magnitude of lateral gradients through stirring and increased the potential for Ekman-driven cross-frontal flow to modulate the stability of the mixed layer and mixed layer properties. The inclusion, particularly of submesoscale Ekman Buoyancy Flux parameterizations, in coupled-climate models, may improve the representation of mixed layer heat and freshwater transport in the ice-impacted Southern Ocean during summer.

Plain Language Summary

Sea ice melt around Antarctica is an annual event in which the state of the surface ocean is transformed, during which over 15 trillion litres of freshwater enters the upper ocean. This fresh layer separates the upper ocean from the deep ocean and suppresses the exchange of heat and gases - like carbon dioxide - between the deep ocean and the atmosphere, with important implications for the climate system. Because of the sparsity of high-resolution observations, the ability of current climate models to accurately represent this region is likely reduced. Using state of the art autonomous underwater gliders we observed key physical properties of the surface ocean following the melt of sea ice. The presence of fine scale fronts (sharp changes in density), of less than 10 km in horizontal scale, revealed that sea ice melt not only stabilizes the upper ocean, but also pro-

vides energy for small eddies to form. While the eddies are unable to extend deeper than the fresher surface layer, they enhance the ocean response to winds. These findings may contribute to the improvement of global climate models and our understanding of how the ocean will react to changes in sea ice under a warmer climate.

1 Introduction

Around Antarctica, sea ice forms a relatively thin (~ 1 m) insulative layer over the ocean's surface, covering an area of ~ 19 million km^2 (roughly equivalent in size to the Antarctic continent itself) and retreating to an area of ~ 3 million km^2 in summer (Parkinson, 2014). This expansion and contraction of sea ice is important for Southern Ocean heat uptake since it modulates the transfer of heat between the atmosphere and deep waters through its influence on the salinity and density of the surface waters (Bitz et al., 2006; Kirkman & Bitz, 2011). However, climate models continue to diverge in their representation of heat and carbon exchange in the Southern Ocean (Frölicher et al., 2015). With the paucity of observations south of 50°S (Newman et al., 2019; Swart et al., 2019), it is likely that some of the model uncertainties can be attributed to misrepresented atmosphere-ocean processes associated with the sea ice-impacted Southern Ocean (Chemke & Polvani, 2020).

The seasonal melt of Antarctic sea ice is the primary source of freshwater in the Southern Ocean south of 50°S (Abernathy et al., 2016). When the melting of sea ice occurs in the spring, freshwater (more than 15 trillion liters) is reintroduced into the surface waters and advected by Ekman processes (Speer et al., 2000) northwards. This phenomenon is associated with a net freshening and lightening of the mixed layer (ML) (Pellichero et al., 2017). Through the resultant impact on water mass transformation (Abernathy et al., 2016), the ice-impacted ML acts as a conduit between sea ice dynamics and the global ocean circulation (e.g., Haumann et al., 2016; Pellichero et al., 2018).

At the northern edge of the sea ice, a dynamic band of low concentration sea ice defines the Marginal Ice Zone (MIZ), separating the open ocean from the ice pack. One-dimensional mixing processes associated with local sea ice melt and vertical mixing have been shown to dominate upper ocean physics in MIZs (Dewey et al., 2017; Smith et al., 2018). However, it has been demonstrated by theory and models that submesoscale flows in MIZs interact with horizontal gradients in density to modify ML structure, (Horvat

et al., 2016; Lu et al., 2015; Manucharyan & Thompson, 2017), and by observations in the Arctic (Timmermans & Winsor, 2013; Koenig et al., 2020; Brenner et al., 2020) and more recently in the Antarctic (e.g. (Swart et al., 2020; Biddle & Swart, 2020)).

Mixed layer baroclinic instabilities (MLI, (Fox-Kemper et al., 2008)), a class of sub-mesoscale flows, are characterized dynamically by order one Richardson and Rossby numbers (Thomas et al., 2013; McWilliams, 2016). MLI give rise to mixed layer eddies (MLEs), which can increase surface stratification through an eddy overturning and induce large vertical velocities and fluxes. In this way, surface stratification is influenced both diabatically through heat gain and loss to the atmosphere, and adiabatically, through the dynamical restratification by frontal slumping. While a range of submesoscale flows can impact surface boundary layer variability, MLEs, associated with baroclinic instabilities, are ubiquitous in the surface ocean.

MLI have the potential to structure the upper ocean in sea ice-impacted regions. A combination of simulations and observations by Horvat et al. (2016) and Lu et al. (2015) show MLI can be formed from freshwater fronts by melted sea ice and result in the horizontal mixing of heat, enhancing the melt of nearby ice floes. Similarly, Manucharyan and Thompson (2017) model MLI which feed off existing frontal structures in a MIZ. The submesoscale structuring of fronts and filaments leads to intermittent fluxes of heat and sea ice which can contribute to the structuring of the upper ocean in MIZs. MLEs, which grow from the MLI, may contribute to the flux of underlying warmer water to the surface. Adding a layer of complexity, von Appen et al. (2018) propose that subduction associated with baroclinic instabilities and ML fronts is enhanced due to increased mixing from cabbeling - when two water masses of the same density mix and the resultant water mass is denser. MLEs tend to give rise to increased stratification, however, Brenner et al. (2020) could not conclusively show that eddies formed from baroclinic instabilities were a leading factor in setting the ML stratification. This study suggests that MLEs may not be sufficiently strong in MIZs to impact upper ocean stratification. The results from ice-covered (Timmermans et al., 2012) and ice-free (Timmermans & Winsor, 2013) Arctic MIZ observational campaigns provide evidence for submesoscale restratification, albeit with potential density spectral slopes steeper (k^{-3}) than the open ocean mid-latitudes (k^{-2}), suggesting that different physical mechanisms are controlling the horizontal structure of the upper ocean compared to mid-latitudes. In the Antarctic, evidence of active MLI has been observed (Biddle & Swart, 2020), even under suppressed surface forcing

(reduced wind and solar heat loss from sea ice cover), emphasising the role of sea ice fronts in the production of submesoscale instabilities. While it has been shown that MLI are actively structuring the ML in MIZs - through restratification or lateral and vertical mixing - it remains uncertain in observations whether MLI are strong enough to result in significant vertical fluxes across the base of the ML in the strongly stratified MIZs.

Observations of wind-front interactions in ice-free MIZs yield contrasting results between the studies. Under winter conditions near the Arctic MIZ, Koenig et al. (2020) provide evidence of sustained turbulence by forced symmetric instabilities associated with downfront winds and heat loss from the surface layer, which extract potential vorticity from the water column at submesoscale fronts. Conversely, Brenner et al. (2020) found that upfront winds lead to frontogenesis on time scales shorter than Ekman dynamics. The Antarctic MIZ differs from the Arctic in that the Antarctic sea ice sector experiences strong, event scale storms (Patoux et al., 2009; Vichi et al., 2019). Swart et al. (2020) suggest that in the stormy conditions of the Antarctic MIZ, wind forced thermohaline shear dispersion, in combination with slumping by MLEs, act to reduce the strength of freshwater surface layer fronts. When the winds subside, fronts are able to reform by the stirring of the fresher surface layer by mesoscale eddies and therefore persist well into the summer.

Submesoscale motions and instabilities are seasonal across the world’s oceans, with stronger flows under winter/low ML stratification conditions (Callies et al., 2015). In the Antarctic MIZ during summer, solar heating and freshwater input from bulk sea ice melt both act to stratify the surface layer (Swart et al., 2020), similar to other freshwater driven systems (e.g. Gulf of Mexico; Luo et al., 2016). However, while the freshwater influx stratifies the ML, the dispersing freshwater, originating from sea ice melt, also introduces mesoscale fronts from which submesoscale instabilities can form. The dynamic nature of the Southern Ocean surface layer, influenced by strong winds and passing storms, maintains stratification weaker than otherwise. This sets up an unique interplay between submesoscale ML fronts, stratifying 1D ocean-atmosphere buoyancy fluxes and destratifying mechanical mixing by winds. Dissecting these interactions and their seasonal evolution is the topic of this paper.

The preceding research suggests that properties of the surface layer in polar MIZs is not driven purely by one-dimensional processes. Here, we hypothesise that the per-

sistence of submesoscale activity in the ice-free Antarctic MIZ is associated with northwards advecting freshwater from sea ice melt. We use high resolution *in situ* data in combination with satellite and reanalysis products to interrogate the evolution of the ML in the Antarctic MIZ, from immediately after sea ice melt to the end of summer.

2 Data and Methods

2.1 Study Region

The Robotic Observations and Modeling of the Marginal Ice Zone (ROAM-MIZ) project (2019-2023) involves a field campaign set in the Antarctic MIZ, south of the Southern Boundary of the ACC (Figure 1a), with a key objective of characterising the role of submesoscale flows on stratification, air-sea fluxes and mixed-layer-interior exchange in the sea ice-impacted Southern Ocean. Satellite color imagery (from the 7th January, at a nominal spatial resolution of ~ 0.3 km, Figure 1b) reveal surface chlorophyll concentrations that suggest the presence of both mesoscale and submesoscale variability. The study region is covered entirely by sea ice during the winter (Figure 1d).

The maximum and minimum sea ice extent for the 2018-2019 season occurred on the 3rd September 2018 and 23rd February 2019, respectively (computed as the maximum integral of pixels with a sea ice concentration > 0.15 from AMSR2; Figure 1a,d). The surface ocean is impacted by ocean-atmosphere buoyancy fluxes (here confined to surface heating defined as the sum of shortwave, longwave, latent and sensible heat, plus Evaporation-Precipitation; refer to section 2.4 for a more detailed explanation of the data used). At the ROAM-MIZ site, ocean-atmosphere buoyancy fluxes peak on the 25th December at 256 W m^{-2} , largely attributable to incoming solar heat (Figure 2a,b). Precipitation events occurred throughout the summer season (Figure 2b). The mean wind stress is $0.09 \text{ N m}^{-2} \pm 0.08 \text{ N m}^{-2}$ with three wind events (storms) reaching $0.4 - 0.6 \text{ N m}^{-2}$ (Figure 2c). Wind direction was variable, but predominantly westerly.

2.2 Seaglider mission and data processing

A Seaglider was deployed at 60°S , 0°E , 445 km south of the Southern Boundary of the Antarctic Circumpolar Current (ACC), estimated using the criteria of Swart et al. (2010), based on contours of SSH (Figure 1b). The deployment commenced in early summer (14th December 2018), just four days after the melt of sea ice when the surface

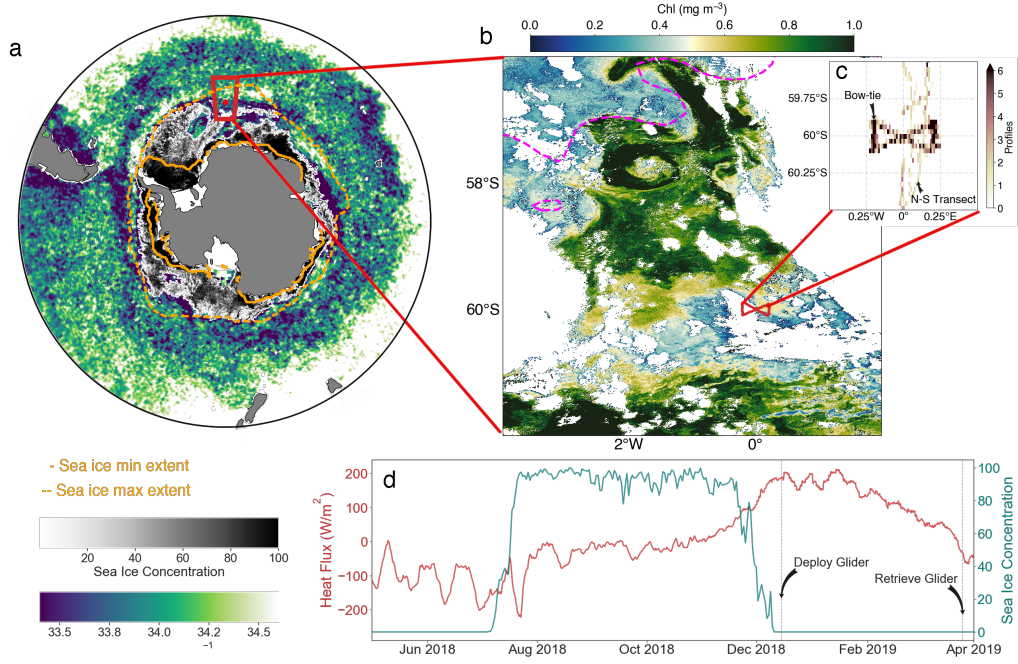


Figure 1. Figure 1: a) Regional view of the ROAM-MIZ study site, showing SMOS salinity on the 16th December 2018, and the sea ice concentration at the time of deployment (14th December 2018). Maximum and minimum sea ice extent for the year 2018-2019 are contoured in dotted and solid orange lines respectively. b) A snap-shot of Sentinel-3A OCLI Chlorophyll Ocean Colour in cloud free conditions on the 6th January 2020, during the deployment. The Southern Boundary of the ACC is demarcated by the dashed magenta line. The deployment is marked by the red bow-tie, reflecting the sampling pattern that was maintained for the duration of the deployment. c) Heat map showing the spatial distribution of profiles captured by the Seaglider. d) Annual time series of net downward heat flux and sea ice concentration at 60°S, 0°E. The time of deployment and retrieval of the Seaglider is indicated by the black arrows.

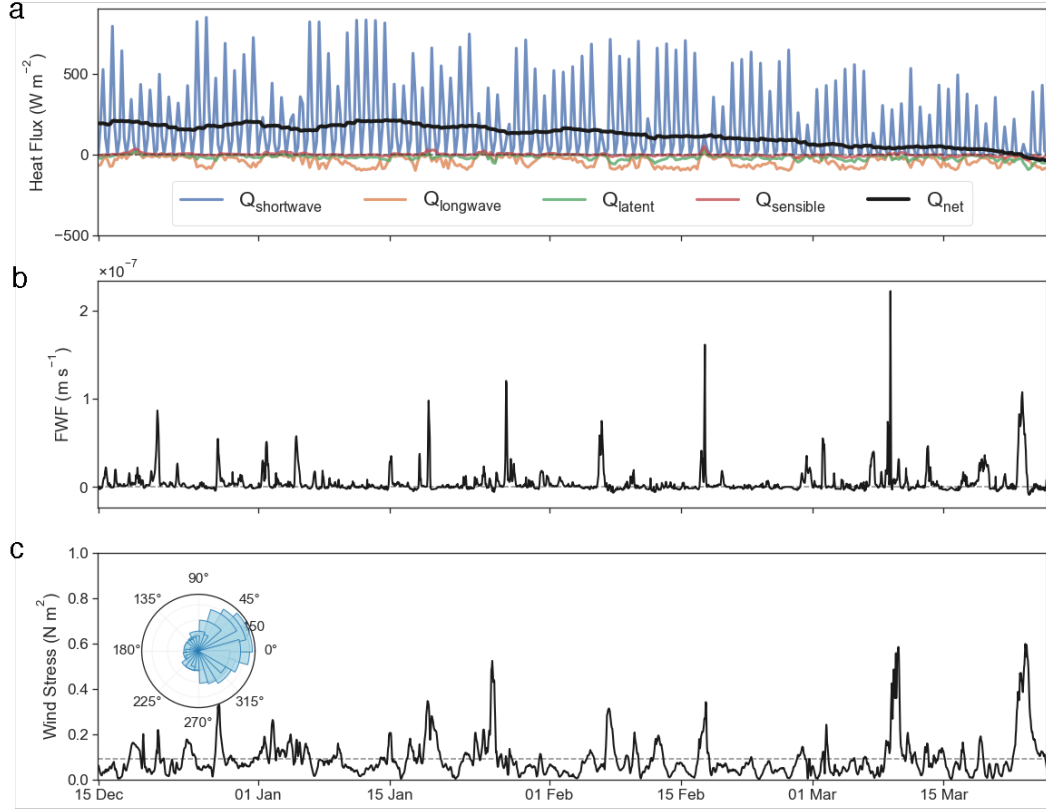


Figure 2. Summer time series of surface forcing from ERA5 reanalysis at the ROAM-MIZ site between December 2018 and March 2019. a) surface heat flux decomposed into its components: shortwave, longwave, sensible and latent heat flux with the sum of components, the net surface heat flux plotted in black. A running mean of 24 hours is applied to the net surface heat flux, b) surface freshwater flux (E-P) and c) wind stress with the distribution of the wind direction inset. The average wind stress is marked with a grey dashed line.

heat flux into the ocean was almost at its maximum (Figure 1d), and continued for 102 days, until the 26th March. The Seaglider was piloted in a ‘bow-tie’ sampling pattern completing repeat transects of approximately 20 km in length. The bow-tie sampling strategy was adopted to best observe the isotropic lateral gradients at submesoscales and thus provide a statistical representation of the lateral gradients in the region (see section 2.5). To assess the background mesoscale field, at the start and middle of the mission, two north-south mesoscale transects (185 km and 120 km, respectively) were completed. In total, the Seaglider covered a distance of 2074 km, collecting 974 profiles, 1000 meters in depth. Noting that Seagliders sample in both time and space, for the analysis we interpret the data in a Eulerian sense, similar to the approach used by du Plessis et al. (2019).

The Seaglider sampled temperature and conductivity (salinity) nominally at 0.2 Hz, equating to a vertical resolution of 0.2-1.5 m, with an average resolution of 0.5 m in the upper 400 m. The Seaglider data was prepared for analysis using GliderTools (Gregor et al., 2019). Salinity and temperature were converted to absolute salinity and conservative temperature respectively, using the Gibbs Seawater toolbox (McDougall & Barker, 2011). Finally, the Seaglider conductivity and temperature data were corrected against the calibrated shipborne data from conductivity-temperature-depth (CTD) casts at the deployment and retrieval of the Seaglider (as per Swart et al. (2015)). The mixed layer depth (MLD) is calculated from the Seaglider data using the density difference criteria of 0.03 kg m^{-3} from a reference depth of 10 m (de Boyer Montégut et al., 2004).

2.3 Thermal lag correction of salinity

Small errors in profile-to-profile temperature and salinity estimates can artificially enhance estimates of lateral buoyancy gradients. The accurate estimation of submesoscale fluxes, which are a function of lateral buoyancy gradients, demands minimising instrumental error.

Salinity is inferred from measured conductivity and temperature. A temperature sensor measures seawater temperature outside of the conductivity cell, while a conductivity sensor measures seawater conductivity inside of the conductivity cell. This spatio-temporal mismatch introduces an offset in the temperature of the water that the conductivity sensor actually measures, resulting in thermal lag that needs to be corrected for, to obtain accurate salinity measurements. The presence of thermal lag in data re-

sults in errors in salinity and density, especially at the thermocline where there are sharp gradients in temperature and salinity.

In the case of unpumped CTDs, the vehicle propulsion is what induces flow through the sensor. Thermal-lag effects change as the speed of the vehicle fluctuates, especially across the thermocline and when the vehicle is at apogee. A correction, as described by Lueck and Picklo (1990) and more recently Garau et al. (2011), is applied to the conductivity and temperature sensor in the initial processing. The effectiveness of this correction depends on knowing the speed of the vehicle and therefore the speed of the flow of water through the conductivity sensor, which is reliant on determining a good flight model. Two models are derived: 1) from the change in pressure observed by the vehicle (glider-slope model) and 2) from the change in buoyancy (hydrodynamic model) of the vehicle (Frajka-Williams et al., 2011), which rely on good estimations of the gliders lift, drag, induced drag coefficients, volumes, glider absolute compressibility and glider volumetric thermal expansion. The accuracy of these variables is reliant firstly on pre-deployment measurements and initial piloting procedures, and secondly by minimising error in the flight model (e.g. regressing the glider-slope model with the hydrodynamic model, as implemented in the UEA-GliderToolbox¹).

Error induced in the data by thermal lag is particularly pertinent in waters where the density is set by salinity; this is because salinity is most affected by thermal lag, with the correction resulting in a root mean square error of $4 \times 10^{-3} \text{ g kg}^{-1}$. An analysis of the offset between climb and dive and dive and climb profiles during the deployment, highlights the regions where thermal lag most affects the data (Figure 3).

To constrain the error in our analysis of submesoscale fluxes we quantify the error contribution to ML lateral density gradients by thermal lag. We compute the difference between dive-climb (climb-dive) dives between the surface and 15 m above the ML (Figure 3d,h). By inspecting the distribution of all the differences in density between climb and dive profiles we see a skewed distribution to the left (Figure 3d) with the 50th percentile of corrected profiles with an RMSE of $0.005 \text{ kg m}^{-3} \text{ km}^{-1}$ ($0.002 \text{ kg m}^{-3} \text{ km}^{-1}$), indicated by the dashed red lines in Figure 3d and 3h. The error is smaller in the dive-climb dive pairs (Figure 3h) because the distance between the profiles is larger. The skewed

¹ <http://www.byqueste.com/toolbox.html>

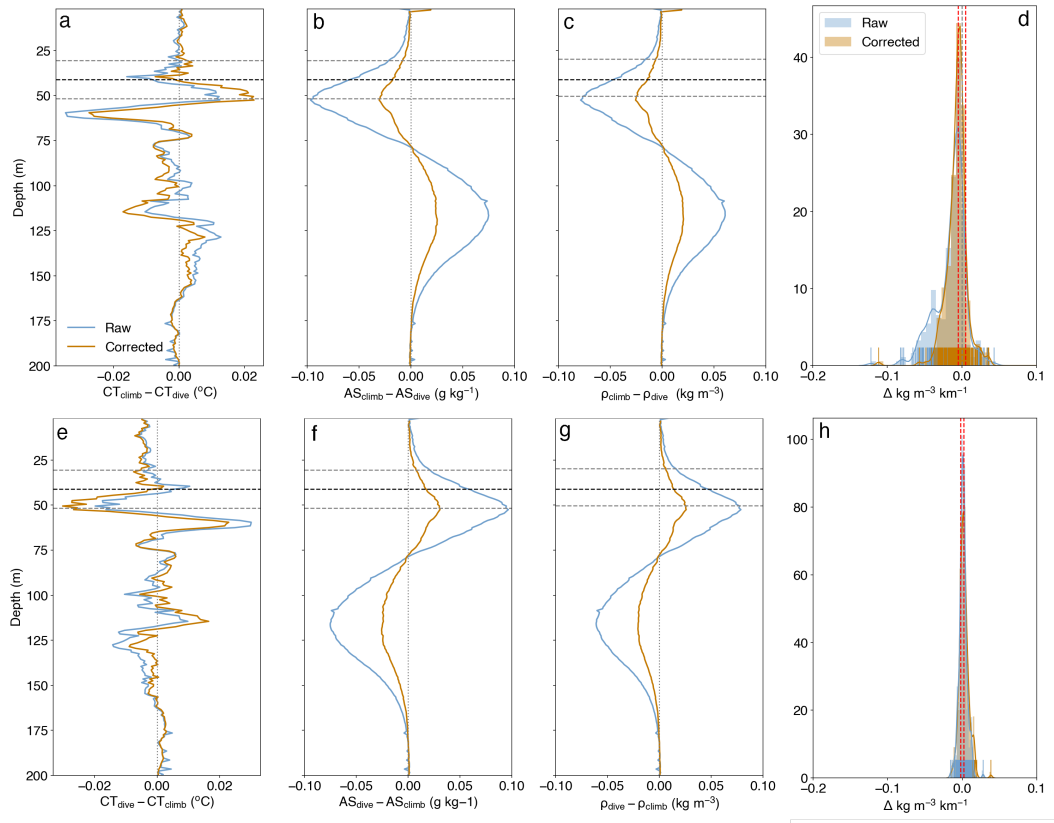


Figure 3. Seaglider uncorrected and thermal lag corrected a,e) conservative temperature (CT), b,f) absolute salinity (AS) and c,g) density (ρ). The mean and standard deviation of the ML depth is indicated by dashed lines. d,h) Distribution of the salinity differences between the surface and 15m above the MLD between all climb and dive Seaglider profiles. a-d) Climb-Dive e-h) Dive-Climb

error suggests the presence of weak thermal lag error between the surface (2 m) and 15 m above the MLD. This skewness towards underestimating the salinity is consistent with the Seaglider transiting from a warmer surface layer (cooler winter water) to a cooler winter water (warmer surface layer) on the dive (climb). Lateral density gradients of up to $0.015 \text{ kg m}^{-3} \text{ km}^{-1}$ are captured by the Seaglider, with the 50th percentile residual error after correcting for thermal lag resulting in an overestimation of lateral density gradients per km by 7 % on the dive/climb pairs and 17 % on the climb/dive pairs. Altogether, the overestimation of lateral gradients due to thermal lag is likely counterbalanced by the fact that gradients are underestimated because the Seaglider does not sample fronts perpendicularly (see section 4.5.1).

2.4 Atmospheric Reanalysis and satellite data

Surface forcing was obtained from ECMWFs (European Centre for Medium-Range Weather Forecasts) ERA5 reanalysis. Wind stress was computed from meridional and zonal winds at 10 m height. Net surface heat fluxes (Q_{net}) were computed from short-wave and longwave contributions, as well as latent and sensible heat fluxes. Net freshwater fluxes (FWF) were computed as Evaporation-Precipitation. Sea ice fluxes are not included because the region was sampled after the sea ice had melted. For comparison to Q_{net} , FWF is first converted to a surface buoyancy flux and then to an equivalent heat flux with the following equation:

$$Q_{FWF} = \rho_0 C_p \frac{\beta}{\alpha} S_{surf} (E - P), \quad (1)$$

where g is gravity, $\rho_0 = 1027 \text{ kg m}^{-3}$ is a reference density, $C_p = 4000 \text{ J K}^{-1} \text{ kg}^{-1}$ is the heat capacity of water, $\alpha = 5.7 \text{ K}^{-1}$ is the thermal expansion coefficient of water and $\beta = 7.8 \times 10^{-4} \text{ kg g}^{-1}$.

The sea surface height fields used to determine the location of the Southern Boundary of the ACC are based on SSALTO/Duacs Maps of Absolute Dynamic Height (MADT). Daily sea ice concentration from AMSR2 (Spreen et al., 2008), with a 6.25 km lateral resolution, was used in this study. The sea ice sector of the Southern Ocean was defined by the winter maximum of sea ice, with sea ice concentration greater than 15 %. The regional maps of salinity are produced from ESA's Soil Moisture Ocean Salinity (SMOS) Earth Explorer mission using de-biased Sea Surface Salinity L3 v4 maps that were generated by LOCEAN/ACRI-ST Expertise Center (Boutin et al., 2018). The global standard deviation of SMOS is 0.20 psu in the open ocean, compared to 100 km-averaged ship SSS, but in polar seas this is increased. Acknowledging this, we use SMOS only to characterise the regional impact of sea ice on salinity, rather than relying on the actual magnitude in salinity. The surface chlorophyll map was produced with Level 2 data from the Copernicus Sentinel-3 Ocean and Land Colour Instrument.

2.5 Buoyancy gradients

Along-track (as measured by the Seaglider) time series of buoyancy were calculated as

$$b = g(1 - \rho/\rho_o). \quad (2)$$

The contribution of temperature and salinity to the magnitude of lateral (along-track) density gradients was computed as:

$$b_x = g\alpha \frac{\partial T}{\partial x} - g\beta \frac{\partial S}{\partial x}. \quad (3)$$

By design, Seagliders sample in a ‘saw tooth’ pattern as they propel themselves through adjusting their buoyancy. This results in ML ($z \sim 10 - 40$ m) profiles which are captured at high resolution ($x \sim 300$ m) between a climb profile and a dive profile, and profiles which are further apart ($x \sim 4$ km) between a dive profile and a climb profile. An in-depth analysis of the implications of this sampling pattern in capturing lateral gradients in the ML is provided by (Swart et al., 2020) (see their Supplementary Figure 2).

The calculation of lateral buoyancy gradients $\frac{\partial b}{\partial x}$ and associated submesoscale fluxes necessitated interpolation onto a uniform grid. For this analysis, along-track measurements of temperature and salinity, after binning to 1 m vertical bins, were linearly interpolated onto a uniform grid of $\partial x = 1$ km, from which density and buoyancy were computed. The ML lateral buoyancy gradient is computed as the along-track average buoyancy between the surface (2 m) and 15 m above the ML (~ 25 m) to reduce the error induced by thermal lag (see discussion in section 2.3).

2.6 Stratification and Turner angle analysis

The Brunt-Väisälä frequency is computed and decomposed into contributions from temperature and salinity using the following formulation:

$$N_{ts}^2 = \frac{\partial b}{\partial z} = g\alpha \frac{\partial T}{\partial z} - g\beta \frac{\partial S}{\partial z}. \quad (4)$$

The relative influence of temperature and salinity on vertical density stratification (N^2) is quantified with the Turner angle, which is defined as $Tu = \arctan(R_p)$, using the density ratio $R_p \equiv \alpha \frac{\partial T}{\partial z} (\beta \frac{\partial S}{\partial z})^{-1}$ (Turner, 1973). $\frac{\partial T}{\partial z}$ and $\frac{\partial S}{\partial z}$ are the vertical derivatives

of temperature and salinity. The Turner angle is positive when temperature and salinity have competing effects on density stratification. For $Tu = \pi/4$, temperature stratification is fully compensated by salinity stratification. For $Tu = -\pi/4$, salinity and temperature contribute equally to the density stratification. Salinity stratification exceeds the contribution from temperature stratification when $-\pi/4 < Tu < \pi/4$, and temperature stratification dominates when $|Tu| > \pi/4$.

Similarly, a horizontal Turner angle can be defined by replacing the vertical gradient in temperature with a horizontal gradient. In this way the temperature and salinity contribution to lateral fronts can be decomposed. Fronts in which the Turner angle is positive are at least partially compensated, with $Tu > \pi/4$ indicating that temperature has a stronger impact on density than salinity. Fronts where $Tu < 0$ are anti-compensated in which salinity and temperature are acting constructively to create differences in density. These situations have the potential to produce strong density fronts; however horizontal density gradients can slump due to gravity and may not persist (Rudnick & Cole, 2011). The horizontal Turner angle is computed using a length scale of 1 km.

To test whether the distribution in the vertical and horizontal Turner angles changes over the course of the summer season, the data is split into the first quartile (early summer) and last quartile (late summer) of the full dataset until the atmospheric heat flux becomes zero. Each quartile consists of 500 data points, equivalent to 22 days and 25 days in early and late summer respectively, a temporal resolution of roughly 1 hour.

2.7 Submesoscale Equivalent Heat Fluxes

The non-dimensional Richardson number ($Ri = \frac{N^2}{(\partial u / \partial z)^2} = \frac{f^2 (\frac{\partial x}{\partial z})^2}{N^2}$), which provides a ratio between vertical stratification and geostrophic shear, characterizes the dynamic regime where large values, $Ri \gg 1$, represent quasi-geostrophic flow and small values, $Ri \approx 1$, an ageostrophic regime where submesoscale flows may be active. Using Seaglider observations, we apply the thermal wind assumption such that geostrophic shear is given by the squared along-track lateral gradient normalised by the Coriolis acceleration to give the bulk Richardson number, $Ri_b = \frac{f^2 N^2}{b_x^2}$.

MLI develop through cross-frontal motion that results in the stretching or compression of fluid parcels. Because vorticity is conserved during this process, there is an inverse cascade of energy and eddies are formed (referred to as mixed layer eddies (MLEs)),

that typically manifest at horizontal scales $O(0.1-10 \text{ km})$ and can induce vertical velocities of $O(100) \text{ m day}^{-1}$ (Boccaletti et al., 2007) by converting horizontal buoyancy gradients into vertical gradients. This overturning of density surfaces restratifies the water column and can be expressed in terms of a vertical stream function (Fox-Kemper et al., 2008):

$$\psi_{MLI} = 0.06 \frac{\mu(z) b_x H^2}{|f|}, \quad (5)$$

where μ , represents the vertical structure and is set to unity for simplicity. The vertical buoyancy flux associated with the MLI stream function can be represented as an equivalent heat flux, (Mahadevan et al., 2012):

$$Q_{MLE} = 0.06 \frac{b_x^2 H^2}{|f|} \frac{C_p \rho_0}{\alpha g}, \quad (6)$$

where 0.06 is an empirically-defined coefficient determined by numerical models (Fox-Kemper et al., 2008) and b_x is the along-track buoyancy gradient. Because the MLI parameterization by Fox-Kemper et al. (2008) is based on the assumption that MLI grow from the potential energy stored in mesoscale lateral gradients, we applied a rolling window of 8km (~ 4 times the internal Rossby radius of deformation) such that the Q_{MLE} values estimated here are based on the mesoscale field.

While Q_{MLE} is always positive and acts to restratify the ML, cross frontal Ekman-driven flow by overlying wind fields result in lateral density advection. In particular, surface wind stress oriented downfront, or in the direction of the geostrophic shear, produces an Ekman transport that advects less buoyant over more buoyant water, a condition that is gravitationally unstable and induces turbulent mixing, arresting re-stratification. This mechanical surface forcing can, similarly to MLI, be expressed as an equivalent heat flux, referred to as Ekman Buoyancy Flux (EBF), which involves the component of the wind stress aligned with the submesoscale front (Thomas & Lee, 2005; D’Asaro et al., 2011):

$$Q_{EBF} = -\frac{b_x^2 \tau^y}{f} \frac{C_p \rho_0}{g}. \quad (7)$$

In calculating the along-front (across-track) wind stress, the wind will not always be aligned with the surface fronts. Following (Viglione et al., 2018), the winds were ro-

tated relative to the Seaglider orientation to determine the wind stress component perpendicular to the Seaglider's trajectory (τ^y). Negative values of Q_{EBF} correspond to destabilizing, down-front conditions.

For this analysis, we assume the Ekman layer is equivalent to the MLD. This assumption simplifies the vertical structure of the upper ocean. While we acknowledge this is a non-trivial assumption, the equivalence of the MLD and the Ekman layer is perhaps reasonable under these summer conditions, when the ML is shallow and the winds are strong. A scaling analysis of the Ekman depth based on a κ_d , the turbulent diffusivity, $\sim 0.1 \text{ m}^2 \text{ s}^{-1}$, gives an Ekman depth ($H_E = \sqrt{2\kappa_d/f}$) of about 40 m, which is the average MLD of the upper ocean in these observations.

A case study is presented to contextualise the results described later in this paper. A subset of the Seaglider observations (with the Seaglider moving both in the southward direction and the northward direction) and winds from which the submesoscale processes of MLI and EBF is computed is shown in Figure 4. EBF is positive (restratifying) under conditions where the across-track winds are oriented upfront. Upfront winds are defined when the across-track winds and along-track b_x observed by the Seaglider have the same sign. For example, during the northward transect, negative b_x and negative τ^y indicate lighter, more buoyant water to the south in combination with westerly winds. In the southern hemisphere, westerly winds result in Ekman transport to the north, pushing lighter water over denser water and restratification.

3 Results

3.1 Mixed Layer Properties

The ML properties evolve over summer from cold and fresh (34 g kg^{-1} , $-1.2 \text{ }^\circ\text{C}$), to warmer and saltier ($1.5 \text{ }^\circ\text{C}$, 34.2 g kg^{-1} , Figure 5). A cold, relatively salty Winter Water (WW) layer, defined as the temperature minimum layer below the 1027.5 kg m^{-3} isopycnal, separates the ML from the warm and salty upper Circumpolar Deep Water (uCDW) at the 1027.7 kg m^{-3} isopycnal (see supplementary figure, S1). Four days after the complete melt of sea ice, the surface layer had shoaled from $\sim 100 \text{ m}$ (observed by a nearby SOCCOM float, see supplementary figure S2) to 41.0 m , gradually deepening to 80 m over the three month glider deployment.

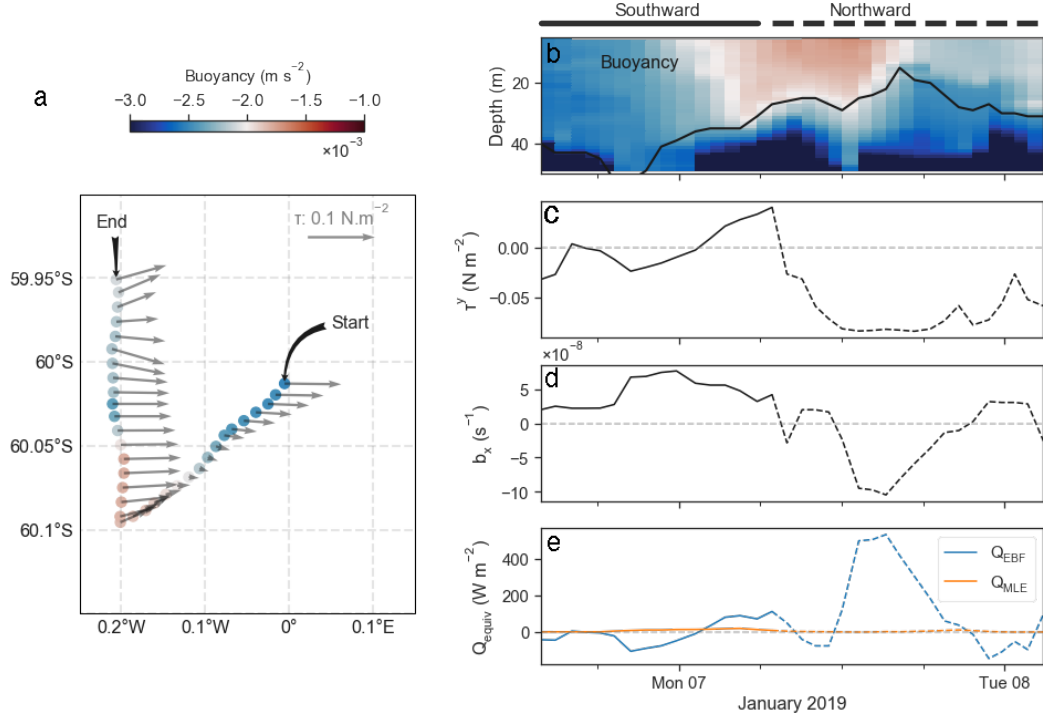


Figure 4. Case study of Seaglider observations during which a strong lateral gradient was sampled. a) Glider trajectory, colored by the buoyancy at 15 m. Black arrows indicate the start and end of the subsample. Wind stress vectors are overlaid in grey. b) Section of buoyancy with the mixed layer depth overlaid in black. c) Wind stress oriented perpendicular to the Seaglider track. d) Along-track buoyancy gradient as observed by the Seaglider. e) Estimated submesoscale equivalent heat fluxes (Q_{equiv}): Q_{MLE} , Q_{EBF} . The solid lines indicate when the Seaglider was moving southwards, while the dashed lines indicate when the Seaglider was moving northwards.

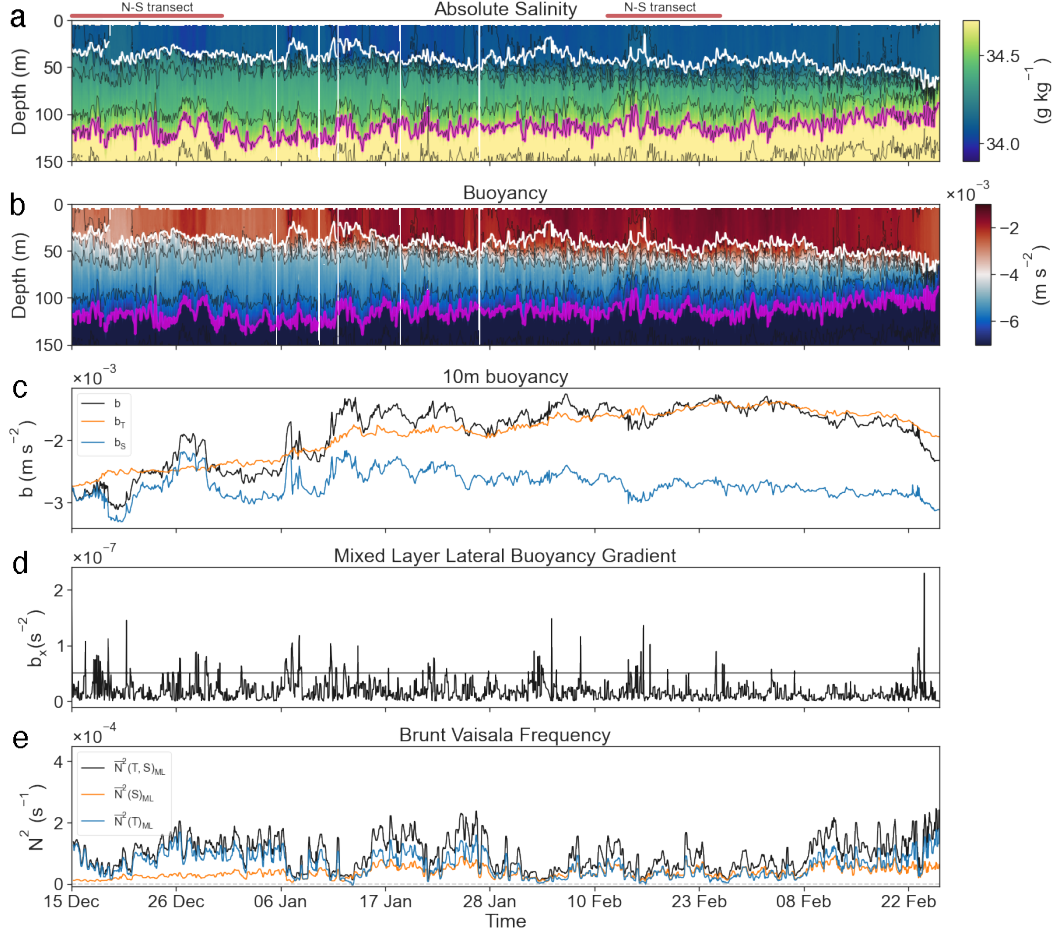


Figure 5. Time series of a) Seaglider sampled absolute salinity. Thin black lines denote density isopycnals with an interval of 0.01 kg m^{-3} . The mixed layer depth is shown in white. The lower bound of Winter Water is marked with magenta lines, identified by the density isopycnal $= 1027.7 \text{ kg m}^{-3}$, the temperature maximum beneath the mixed layer. b) The same as (a) but for buoyancy. c) Temperature and salinity contribution to ML buoyancy (at 10 m depth). d) The average mixed layer buoyancy gradients and e) Temperature and salinity contribution to vertical stratification at the base of the mixed layer. The solid red lines above the plot indicate when the Seaglider was completing mesoscale transects.

ML buoyancy increases from $-3 \times 10^{-3} \text{ m s}^{-2}$ in December to $-1.5 \times 10^{-3} \text{ m s}^{-2}$ by late February, before decreasing again. Buoyancy gradients of up to $1.5 \times 10^{-7} \text{ s}^{-2}$ are observed, equivalent to density fronts of $0.015 \text{ kg m}^{-3} \text{ km}^{-1}$, and salinity fronts of $0.02 \text{ g kg}^{-1} \text{ km}^{-1}$. The largest lateral buoyancy gradients (those greater than $5 \times 10^{-8} \text{ s}^{-2}$, Figure 5d) are observed until mid-February. Early summer is characterized by N^2 values at the base of the ML of $1.1 \times 10^{-4} \pm 4.6 \times 10^{-5} \text{ s}^{-1}$, which decrease in late summer to $6.7 \times 10^{-5} \pm 3.9 \times 10^{-5} \text{ s}^{-1}$. Towards the end of summer, from $\sim 8^{th}$ March, the ML deepens to 80 m, WW isopycnals move closer together, and stratification at the base of the ML increases again to $1.4 \times 10^{-4} \pm 6.6 \times 10^{-5} \text{ s}^{-1}$ in March.

Seaglider observed conditions in the upper ocean are embedded within a larger mesoscale field. In this region, and during the sea ice melt season, the mesoscale field is predominantly structured by northwards advecting freshwater from sea ice melt. The freshwater signal emanating from the melting sea ice, observed in SMOS Sea Surface Salinity (Figure 1a), is mirrored in the Seaglider profiles (Figure 5a) and specifically in the first mesoscale transect (Figure 6a). Low saline water is advected northwards by the predominantly westerly winds. We confirm this by estimating the Ekman component of the salinity tendency budget from lateral salinity gradients observed during the mesoscale transects.

$$\frac{\partial S_{Ekman}}{\partial t} = U_e \cdot \nabla S_m, \quad (8)$$

where,

$$U_e = \frac{1}{\rho_o f H} \begin{pmatrix} \tau^y \\ -\tau^x \end{pmatrix} \quad (9)$$

$\frac{\partial S_{Ekman}}{\partial t}$ is computed by taking an average across-track wind stress of 0.09 N m^{-2} to the east (note that the wind stress varies synoptically and not seasonally), and the large scale gradient across the two mesoscale transects shown in Figure 6. The Ekman contribution to the upper ocean salinity tendency is larger than or comparable to the salinity tendency attributable to freshwater flux by evaporation and precipitation ($\frac{\partial S_{Ekman}}{\partial t} \sim 2.1 \times 10^{-8} \text{ g kg}^{-1} \text{ s}^{-1}$ and $\frac{\partial S_{FWF}}{\partial t} \sim 4.8 \times 10^{-9} \text{ g kg}^{-1} \text{ s}^{-1}$). The contribution of S_{ekman} decreases in the second mesoscale transect as the mesoscale lateral salinity gradient decreases (Figure 6b), potentially indicating a decrease in freshwater advection northwards.

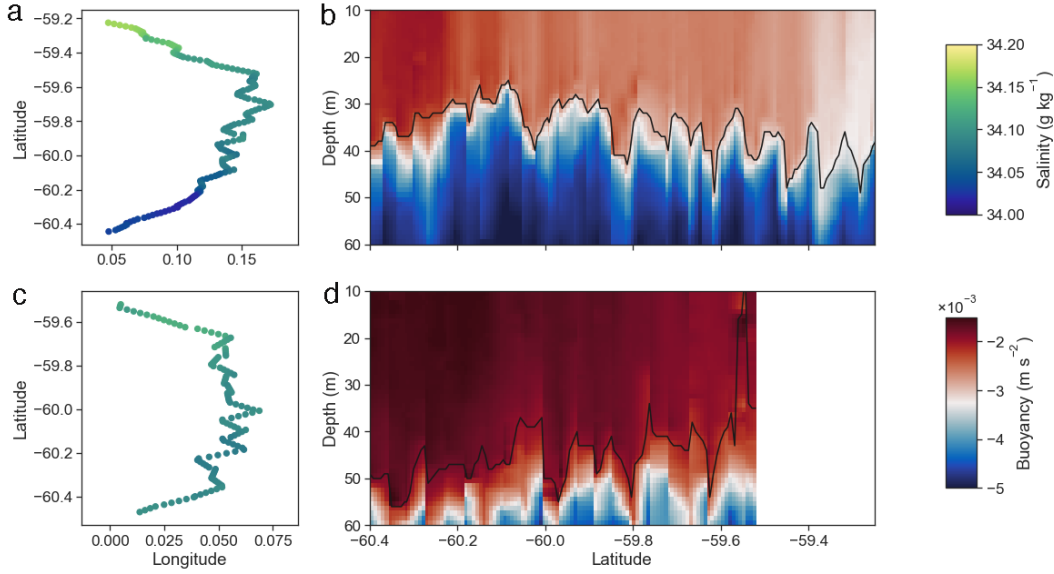


Figure 6. Subset of the Seaglider data showing the mesoscale transects at the beginning (a, b) and middle of the deployment (c, d). Panels a) and c) show the Seaglider trajectory with salinity overlaid. Panels c) and d) are sections of the glider-observed buoyancy. Black lines in panels c) and d) are the mixed layer depth.

3.2 Vertical and lateral stratification

To quantify the contribution of salinity and temperature to ML density, the vertical and horizontal Turner angles were computed. In both cases, the haline contribution to density decreases as the season progresses (Figure 7).

In the vertical, the average Turner angle of the upper 200 m reveals a bimodal structure representing the interface between the surface water and WW, and the interface between uCDW and WW (shown in the time series, Figure 5a, b). In late summer, the distribution of the vertical Turner angle shifts to $-\frac{\pi}{2}$, representing the increased role of temperature in setting vertical stratification.

Similar to the vertical stratification, lateral density variations in the ML are salinity compensated during early summer (Tu distribution centered at zero, Figure 7b), moving towards mixed salinity and temperature compensated fronts towards late summer (distribution broadens).

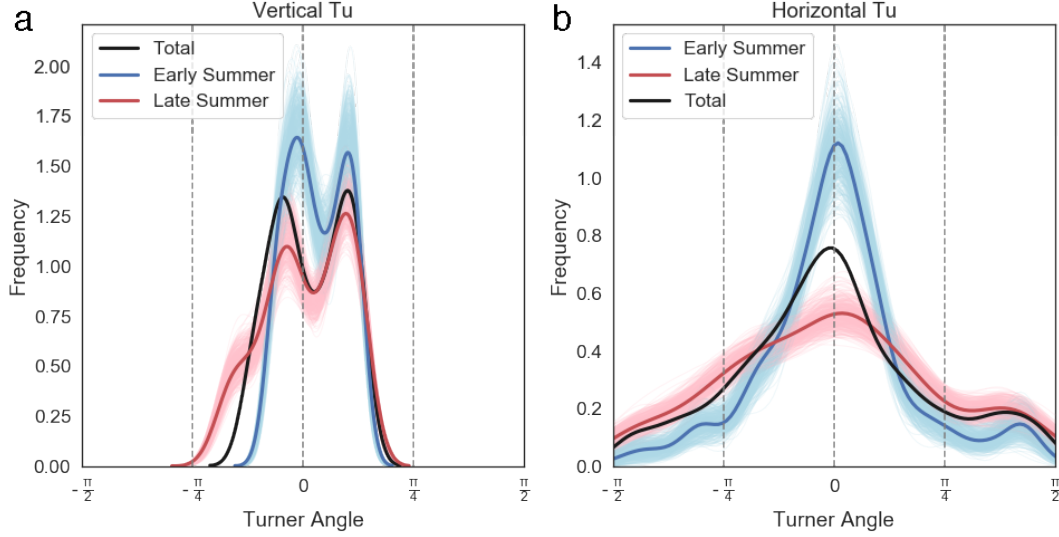


Figure 7. Distribution of the Turner angle in the upper ocean at 60°S, 0°E during summer (black line), decomposed into early summer (blue line) and late summer (red line). a) Histogram of the vertical Turner angle averaged in the upper 200 m. b) Histogram of the horizontal Turner angle. Bootstrapping was applied to the early summer and later summer subsets to give the confidence intervals marked in light blue and pink shading, respectively.

3.3 Submesoscale instabilities and fluxes

Wavenumber spectra are used to describe the horizontal density variance in the surface layer. Typically, spectra with slopes k^{-2} indicate submesoscale variability, while spectra with slopes k^{-3} are more representative of geostrophic regimes (Charney, 1971). The spectra in Figure 8 are computed by removing the seasonal trend from the gridded density data averaged over 10 - 30 m, then averaging the Fourier coefficients in wavenumber bands with more degrees of freedom at higher wavenumbers. The slope of the spectra in Figure 8a is computed from regressing the spectra between 3-20 km, while the slope in Figure 8b, is taken between 3-50 km. We limit the lowest wavelength to 3 km, after which the slope flattens, representing high frequency variability where instrumental noise interference cannot be separated from physical observations (Rudnick & Cole, 2011). The mean slope of all the short (~ 20 km) glider transects is $k = -2.2 \pm 0.76$. Whilst the slope is not consistent between transects, there are more occurrences of $k=-2$ slopes during early summer (mid-December after the mesoscale transects to end-January, 50 % of the transects, $k = -2.08 \pm 0.73$) compared to late summer (February to March, 25 % of the tran-

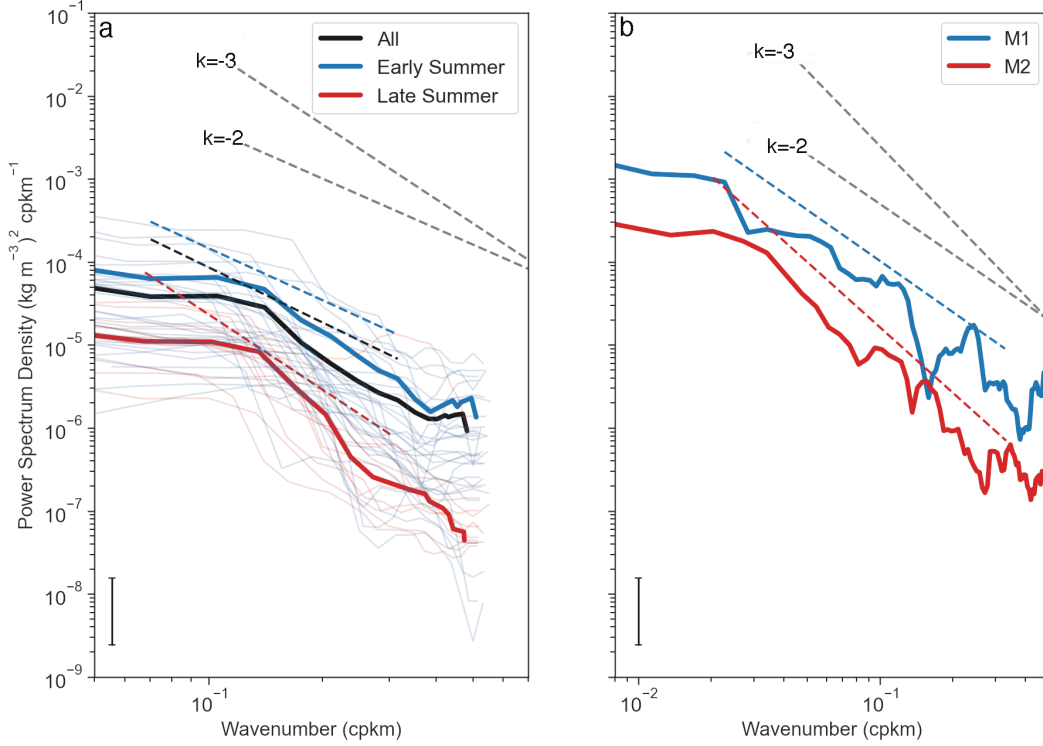


Figure 8. Power spectral density over the average upper 10 m - 30 m for (a) the 20 km transects and (b) mesoscale transects. In (a), the black line is the average spectra from all the transects with a slope of $k = -2.2 \pm 0.76$, the blue line is the average from December to January (early summer, $k = -2.08 \pm 0.73$), and the red line the average of February to March (late summer, $k = -3.0 \pm 1.25$). The blue and red lines split the spectrum into the first mesoscale transect (blue) and the second mesoscale transect (red). The 95 % confidence interval of the spectra is plotted in the lower left corners of each panel. Reference slopes of k^{-2} and k^{-3} are shown by the gray dashed lines and labeled in the figure. The slope in the first mesoscale transect (M1) is $k = -2.0 \pm 0.30$ and $k = -2.6 \pm 0.23$ in the later transect (M2).

sects, $k = -3.0 \pm 1.25$). Moreover, focusing on the spectra itself, the total magnitude of the density variability is smaller and the reduction in variance is greater at smaller scales (at high wavenumbers), later in the summer season. The mesoscale transects from Figure 6 are plotted in Figure 8b. Here, there is a change in slope from $k \sim -2$ to $k \sim -3$ ($k = -2.0 \pm 0.30$ and $k = -2.6 \pm 0.23$ in the first and second mesoscale transects respectively). Note that for each of the slopes in Figures 8a and 8b, a sensitivity analysis to the choice of length scale over which to compute the slope was performed, and did not adjust the magnitude of the slopes significantly (not shown).

We focus our analysis on the potential for MLI to form the submesoscale structure suggested in Figure 8. Conditions where lateral gradients have scales of $O(1)$ km and stratification is weak (Richardson numbers $\sim O(1)$), indicate when the water column is predisposed for submesoscale overturning to occur. We assess the wavelength and growth rate of the fastest growing MLI, defined as (Stone, 1970; Fox-Kemper et al., 2008):

$$l_{max} = \frac{2\pi U}{f} \sqrt{\frac{1 + Ri}{5/2}}, \quad (10)$$

$$\tau_{max} = \sqrt{\frac{54}{5}} \frac{\sqrt{1 + Ri}}{f}, \quad (11)$$

U , is the vertical shear, determined by multiplying H (the MLD) by the geostrophic shear, calculated from the Seaglider derived lateral buoyancy gradient, as $|bx|/f$, under the assumption of thermal wind balance:

$$U \equiv \frac{|b_x|}{f} H.$$

For the ice-free Antarctic MIZ during summer, taking $Ri = 1$, a typical maximum growth rate is 10 hours, using $f \sim 1.26 \times 10^{-4} \text{ s}^{-1}$, the local inertial frequency, with a typical length scale of 1.4 km (using a MLD of 40 m and lateral buoyancy gradient of $1 \times 10^{-7} \text{ s}^{-1}$). These scales are comparable to simulations by Fox-Kemper et al. (2008), in which an MLD = 100 m and $M^2 = 2f^2$, results in $\tau_{max} \sim 16.8$ hours and $l \sim 3.9$ km.

Using the Seaglider measured lateral buoyancy gradient, MLD and Richardson number, we extend the analysis of the MLI growth rate and wavelength to the full time series (Figure 9). Within the ML, the Richardson number varied over several orders of magnitude (Figure 9c), a function of stratification at the base of the ML and the strength of the lateral buoyancy gradients. During the summer season most of the ML flows are characterized by $Ri \gg 1$, influenced by the strong stratification resulting from the recent sea ice melt, $Ri_{ML} \sim 1 \times 10^5$. Intermittently, a combination of weaker stratification and strong lateral buoyancy gradients brings the system towards an ageostrophic regime where $Ri_{ML} < 4$ in 25% of profiles (Figure 9c). The distribution of the magnitude of lateral buoyancy gradients is skewed to the left, with the majority of lateral gradients being weak (Figure 9a). In early summer, the occurrence of strong lateral buoyancy gradients is more frequent than during later summer (Figure 9f). For the same time

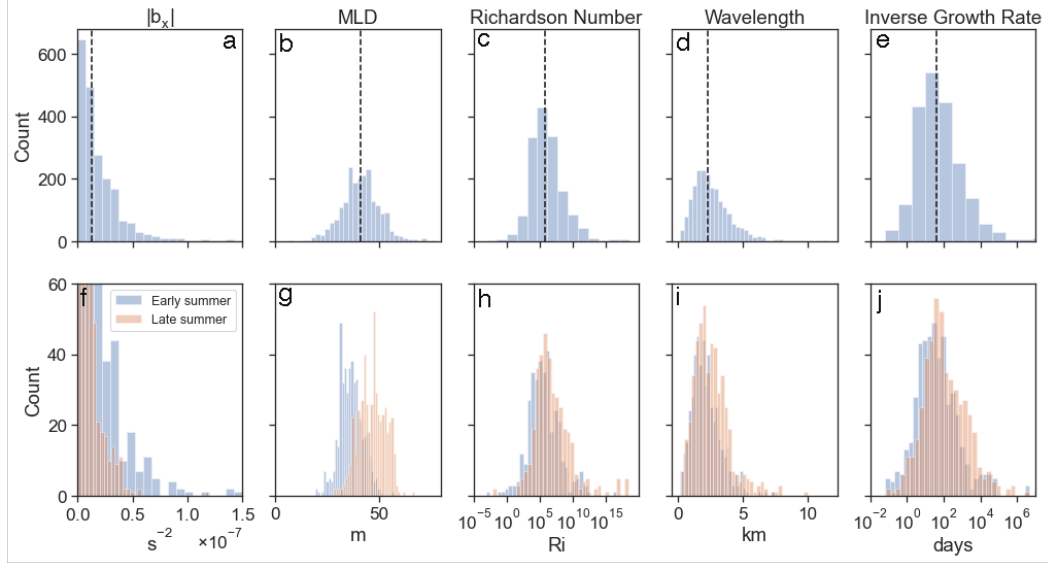


Figure 9. Histograms of : a) Magnitude of along-track buoyancy gradient, b) MLD, c) Richardson Number, d) MLI Wavelength, e) MLI Inverse growth rate. Median values are indicated by the black dashed lines. (f-j) show the seasonal shift in distributions of (a-e) from early summer to late summer using the same definitions as in Figure 5.

period, the distribution of MLD is gaussian (Figure 9b), shifting to a deeper average during late summer (Figure 9g). The majority of the distribution of the wavelength of the fastest growing MLI is typically less than 5 km (Figure 9d), similar to the internal Rossby radius of deformation, $L_r = NH/f = 2 \pm 0.6$ km. The inverse growth rate of MLI is a function of the Richardson number and follows a similar distribution to that of the Richardson number (Figure 9e). The Richardson number, wavelength and growth rate of MLI display a tendency towards higher magnitudes during late summer (Figure 9h-j). Together, these results suggest that the upper ocean undergoes a shift from early summer to late summer in the scales that describe the instabilities and eddies.

Similarly, MLE fluxes and EBF, which both depend on lateral buoyancy gradients, weaken as the summer season progresses and the strength of lateral buoyancy gradients decreases (Figure 10). When MLI is active, their stratifying potential is weak (< 50 W m^{-2}). Conversely, wind interactions with ML fronts have the potential to impact stratification in the ML, with the observed submesoscale fronts ($b_x \sim (O) 5 \times 10^{-8} s^{-2}$), sufficient to induce EBF fluxes greater than 200 W m^{-2} . Together, EBF and MLE increase the variability of the total equivalent heat flux in the ML during early summer by 55 %

(from standard deviation of 35.9 W m^{-2} to 80.5 W m^{-2}), compared to late summer when the influence of submesoscale fluxes is almost negligible, (standard deviation increases from 32.4 W m^{-2} to 34.4 W m^{-2} with the inclusion of submesoscale fluxes) (Figure 10c).

4 Discussion

This study investigates ML dynamics over a summer season in the Antarctic MIZ, in which our three main aims are addressed. First, we investigate whether ML fronts, formed by recent sea ice melt water, remain prevalent during the early summer in the ice free MIZ. Secondly, we characterize submesoscale flows as the summer season progresses and thirdly, we evaluate their impact on the structure of the ML, such as its depth and stratification.

4.1 A salinity-driven system

We find a shift from salinity-dominated to mixed salinity/temperature controlled buoyancy variability through the progression of the summer season. Salinity-driven buoyancy variability is expected in the ice-impacted Southern Ocean where sea ice derived waters drive the seasonal ML salinity budget (Pellichero et al., 2017). Similar occurrences are observed in the Arctic MIZ, with salinity driving ML density variability during ice-free conditions (Timmermans & Winsor, 2013).

Initially, cold, low saline water is advected through the sample region, and positive buoyancy anomalies, driven by salinity, are observed (Figure 5). Mixed layer buoyancy becomes more sensitive to temperature fluctuations as the summer season progresses. A possible explanation for this decoupling is the decrease in low-saline water present in the sample region (Figure 5a, c) and concurrent increase in the temperature contribution to buoyancy as surface temperatures warm. In early summer, the water temperatures are cold ($< 1^\circ\text{C}$) and thus temperature has a small impact on buoyancy because of nonlinearities in the equation of state. As the water temperatures increase, so too does the thermal expansion coefficient and correspondingly the temperature contribution to buoyancy. In this region, the largest contributor to positive surface buoyancy flux is solar heating. Increased buoyancy associated with a warmer ML increases the stability of the ML, with the potential to suppress MLI.

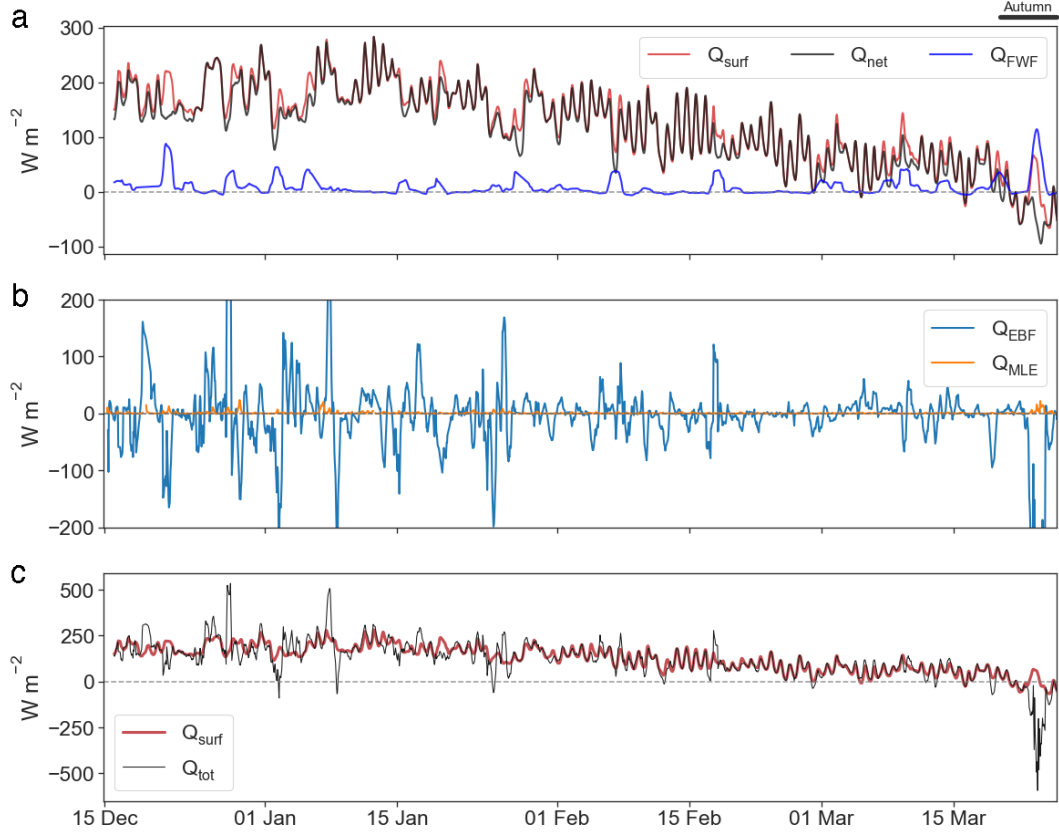


Figure 10. a) Summer surface heat flux (Q_{net} , red) and equivalent freshwater flux ($Q_{\text{freshwater}}$, blue) expressed as an equivalent heat flux from ERA5 reanalysis, and the sum of the two (Q_{surf} , black). Rolling means of 24 hours are applied. b) Equivalent heat flux by submesoscale overturning due to mixed layer baroclinic instability (Q_{MLE} , orange) and Ekman Buoyancy Flux (Q_{EBF} , green). A rolling mean of the inertial period (10 hours) was applied to Q_{EBF} to reduce emphasis on sporadic events. c) Sum of the total surface buoyancy forcing, restratification due to mixed layer eddies and wind-driven submesoscale Ekman transport ($Q_{\text{tot}} = Q_{\text{surf}} + Q_{\text{MLE}} + Q_{\text{EBF}}$) expressed as an equivalent heat flux. The red curve shows Q_{surf} as in a) for reference. The onset of autumn is indicated by the black line above the plot, defined by a shift from positive to negative heat flux into the ocean. Note the change in scale on the yaxis.

Temperature determines the seasonal trend in ML buoyancy (Figure 5c), but variations in salinity that continue throughout the season give rise to lateral density gradients. Salinity contribution to buoyancy varies around a stationary mean, reflecting swirling horizontal gradients likely characteristic of submesoscale eddies (McWilliams, 2016), and providing evidence that MLEs may be contributing to the observed lateral buoyancy gradients.

The time series we present here extends beyond that of Swart et al. (2020), in which they show that submesoscale fronts persist into summer in an interplay between thermohaline slumping by winds and frontogenesis. Corresponding with their observations, lateral buoyancy gradients observed here persist from December to February, but eventually reduce in magnitude from mid-February until the end of March when the surface heat flux turns negative (Figure 2) and the supply of freshwater from the south decreases (Figure 6). While the strength of the overlying westerlies does not noticeably diminish, the amount of freshwater available to advect northwards decreases as the sea ice reaches its minimum extent, ~ 1000 km south of the study site (Figure 1a). The dampening of surface lateral buoyancy gradients in late summer may reflect this loss of a source of positive buoyancy anomalies. In summary, our observations support the hypothesis that sharp (e.g. $b_x > 5 \times 10^{-8} \text{ s}^{-2}$, Figure 5c) sea ice meltwater fronts persist in the ice-impacted Southern Ocean after the sea ice has melted.

4.2 Summer submesoscale processes

We observed salinity-driven lateral fronts at submesoscales during summer in the ice free Antarctic MIZ, with increased prevalence occurring with close proximity to the sea ice melt out (occurring at this study site on the 10th December 2018). Concurring with surface observations by Swart et al. (2020), evidence for an active submesoscale regime during early summer is reflected in the ML density variability, representative of potential energy in the ML (Figure 8). As the summer season progresses, the magnitude of density variability decreases and the reduction in variance is greater at smaller scales. The slope of the power spectral density tends towards steeper slopes from $k = -2.08 \pm 0.73$ in early summer to $k = -3.0 \pm 1.25$ in late summer (Figure 8a). The change in density variability across scales and the steepening of this spectral slope suggests a shift in the intrinsic ocean dynamics and overlying forcing mechanisms. Power spectral density slopes illustrate the transfer of energy across length scales. Ageostrophic regimes includ-

ing the submesoscale, flatten the spectral slope (typically scaling as k^{-2}) as these processes can efficiently transfer energy to small scales through turbulent mixing induced by MLI and their interactions with the mesoscale straining field. Submesoscale regimes dominated by baroclinic MLI tend to have spectral slopes k^{-2} during winter, when MLs are deep (e.g Callies et al., 2015). Steeper slopes do not negate submesoscale activity (Timmermans et al., 2012; Timmermans & Winsor, 2013), but are more characteristic of mesoscale driven regimes (e.g Rocha et al., 2016).

Even though a submesoscale regime is evident (Figure 10), we found that if the fine-scale fronts observed reflect stirring of MLEs, their impact on surface stratification is weak ($Q_{MLE} = 5 - 20 \text{ W m}^{-2}$). With an average surface heat flux of 200 W m^{-2} , restratification by MLEs is not large enough to compete. Winds oriented up or down front have impacts on the lifetime of the fronts with implications to mixing and the persistence of fronts. EBF varies between $100 - 1000 \text{ W m}^{-2}$, up to 2 orders of magnitude greater than Q_{MLE} , and often larger than the ambient surface heat flux. EBF acts to intermittently increase stratification or increase mixing. The effect of winds interacting with ML fronts, decreases later in summer. These results indicate that mechanical wind forcing interactions with the observed fine-scale fronts can be important to the mixed layer structure. Estimates of MLI and EBF are slightly larger than that estimated by Biddle and Swart (2020) for the same region during summer ($Q_{MLE} \sim O(10) \text{ W m}^{-2}$, $Q_{EBF} \sim O(100) \text{ W m}^{-2}$), likely linked to their data record only beginning during late summer conditions and the higher resolution of our sampling (0.3-4 km versus $\sim 9 \text{ km}$ in Biddle and Swart (2020)).

North of the Southern Boundary of the ACC, similar submesoscale fluxes have been observed in the regions between the ACC jets. EKE is relatively weak and MLD is $< 100 \text{ m}$ resulting in similar MLE fluxes to this study (du Plessis et al., 2019) but in the energetic Drake Passage MLs are deeper ($MLD > 100 \text{ m}$) and lateral gradients are stronger (up to $3 \times 10^{-7} \text{ s}^{-2}$), providing MLE fluxes that can reach up to 4000 W m^{-2} (Viglione et al., 2018). By definition, MLEs draw more APE from deeper MLDs (Fox-Kemper et al., 2008). The potential for MLE fluxes in our data is thus limited by the relatively shallow summer MLDs. A secondary peak in MLE potential during early autumn in the Antarctic MIZ, concurrent with ML deepening is shown by Biddle and Swart (2020). Similarly, at the end of this dataset, with the onset of autumn and a deepening ML, MLEs begin to increase in magnitude again.

In the Southern Ocean, denser waters are generally located to the south, with lighter waters to the north. The predominantly westerly winds over this meridional gradient in density creates a large scale destratifying EBF over the region. Within the ACC, similar observations of EBF to the present study support this mechanism at the submesoscale as well (du Plessis et al., 2019). Conversely, at the MIZ, after sea ice melt, the meridional gradient is variable as lighter fresher water advects northwards intermittently, resulting in both stratifying and destratifying EBF under similar wind forcing (Figure 10, S3).

These results show that while submesoscale front generation is likely due to mesoscale stirring of freshwater, stratification may be more strongly influenced by wind-front interactions, represented here by EBF. These findings are in line with previous observations in the Weddell Sea (Biddle & Swart, 2020), suggesting that these dynamics are not limited to the year of this study.

4.3 Mixed Layer response to submesoscale flow

It is challenging to infer the impact of submesoscale flow on the ML structure empirically due to the ephemeral nature of submesoscales together with the multiple processes that impact the variability of the MLD. Yet, our summer data provides evidence that submesoscale processes actively modify the ML, but likely do not penetrate below the ML.

The sea ice impacted ML reflects the influence of atmosphere-ocean fluxes, sea ice and internal ocean variability. Here, we have focused on the relative contribution and interactions of atmospheric forcing, sea ice and submesoscale flows to the ML structure. Heat flux into the ocean is the dominant process in setting the mixed layer stratification over the summer season, with a relatively small contribution from evaporation and precipitation (Figure 8a). Nevertheless, ML buoyancy anomalies are driven by salinity changes, even well into the summer season (although the magnitude of the anomalies decreases).

In our study, MLEs have weak stratifying potential over the summer season (Figure 10b). Under summer conditions, when the ML is shallow, there is less available potential energy for MLEs to restratify the upper ocean. Nevertheless, model studies (Callies & Ferrari, 2018) show that MLI are unlikely to be damped out in shallow summer MLs,

even if mixing time scales are short. One possibility is that MLI do grow and lead to re-stratification of the ML in summer after sea ice melt but quickly exhaust the energy fueling their growth.

The significant contribution of EBF to the upper ocean surface equivalent heat flux was observed, particularly in early summer following sea ice melt (Figure 10). In some studies, submesoscale activity under shallow ML conditions have resulted in deepening MLs (Luo et al., 2016; Lévy et al., 2010) due to the increased vertical mixing induced by the fronts that erode the shallow base of the ML. In this study, while we do not test the evolution of the ML structure with and without the inclusion of submesoscale activity, we speculate that the Antarctic MIZ could be responding similarly and observe a gradual deepening of the ML over the summer season. The presence of fine-scale fronts as a result of swirling MLEs may enhance upper ocean mixing through interactions with surface wind stress. Evidence that this may be the case is presented at the end of the observational time series (~ 20 March 2018, Figure 10). A strong wind and precipitation event (Figure 3b,c) occurs over a strong lateral buoyancy gradient ($> 1 \times 10^{-7} \text{ s}^{-2}$), inducing very strong submesoscale EBF ($> 500 \text{ W m}^{-2}$), with the potential to erode the base of the ML and mix the underlying waters into the ML. Similar strength wind events occurred before in the time series (~ 18 Jan 2018 and ~ 10 March 2018), but during those times the lateral buoyancy gradients were weak and thus EBF was not significant. Because of the intermittency of both the passing wind events and the submesoscale MLEs, it is probable that similar events were missed by the observational platform. It could be speculated, that in nearby regions unobserved by the Seaglider, these wind events, in combination with the lateral buoyancy gradients, may be driving local mixing more than if the submesoscale flows were not active (i.e. when the upper ocean is more homogeneous, winds may not have a large impact).

In this paper, we argue that the fine-scale lateral gradients observed are representative of MLEs. The fine-scale fronts may however also be linked to filamentation by mesoscale eddies. To separate ML lateral gradients resulting from MLEs as opposed to filamentation by mesoscale eddies, we computed spiciness in the ML and spiciness along the 1027.7 km m^{-3} isopycnal which lies below the WW layer (Figure 11). A correlation analysis between detrended spice along isopycnals illustrates the convergence of the correlation to almost zero below the WW layer. This emphasises two points: 1) that most of the anomalies observed in the ML were confined to the ML and likely representative of MLEs,

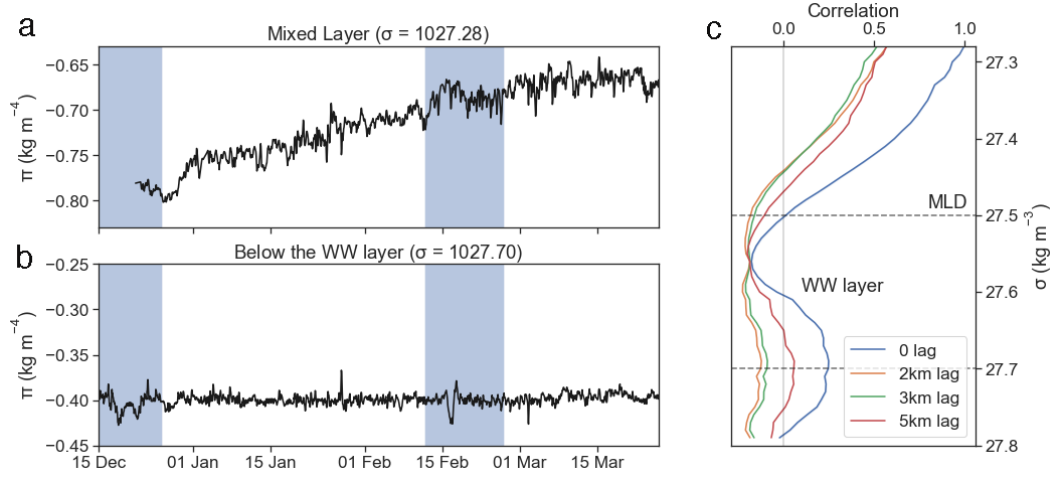


Figure 11. Time series of spice in a) the Mixed Layer and b) an isopycnal below the Winter Water (WW) layer. Blue shading indicates times when the Seaglider was completing the mesoscale transects. c) Correlation between the time series shown in a) and consecutive isopycnals beneath. Dashed grey lines indicate the approximate MLD isopycnal and the isopycnal at the bottom of the WW layer.

and 2) the confinement of MLEs in the ML suggests that there is indeed limited exchange with the interior as a result of sea ice melt which increases upper ocean stratification.

Combined, these results support the hypothesis that the fronts observed are evidence that MLE stirring which effectively brings upper ocean lateral gradients closer together, and the resultant wind-front interactions impact the ML structure during early summer in the Antarctic MIZ. In particular, our evidence highlights the potential role of sub-mesoscale wind-front interactions to maintain weaker early summer stratification at the base of the ML under otherwise highly stratifying conditions.

4.4 Implications

As per Swart et al. (2020), we have shown that submesoscale flow is more active during early summer after sea ice has melted, most likely energised by the regional impact of meltwater fronts, than later in the summer season. Meltwater is an important driver of watermass transformation in the Southern Ocean (Abernathey et al., 2016; Pellichero et al., 2018). In the summer, the shallow ML of the ice-impacted Southern Ocean is subject to transformation through the influx of fresher meltwater, solar heating, stir-

ring by both mesoscale and submesoscale flows and the passage of strong wind events. We find that MLI has low potential to restratify the ML and subduct water to depth. This confirms the necessary advection of these modified waters northward, or potentially downstream in the ACC, before subducting and connecting with the global circulation system (e.g. Figure 1, Pellichero et al., 2018). The substantial increase in the impact of winds on the ML when strong lateral buoyancy gradients or fronts are present, provides a secondary mechanism for eroding the base of the ML and mixing with the underlying warmer and saltier waters. It is interesting to consider whether wind interactions with submesoscale flow play an important role in mixing the uCDW waters into the ML. uCDW waters are warm, salty and high in nutrients, thus the upwards mixing of these waters will act to support primary production as well as modify the properties of the ML. The implications for ML interior exchange in this region under weak MLEs but stronger EBF when submesoscale fronts are active or reduced is an avenue for future research.

Current models and observations indicate that the Southern Ocean is freshening (Haumann et al., 2016, 2020). Even though the ML may become shallower as it becomes fresher, it is likely that MLI will persist (Callies & Ferrari, 2018), and the dynamics described here will continue to be relevant. It has been suggested that the predicted shallower MLs of a warming climate will suppress submesoscale activity (Richards et al., 2020). Here, we show an Antarctic example with evidence of submesoscale activity when the ML is shallow.

4.5 Caveats

4.5.1 Frontal processes observed by gliders

ML lateral buoyancy gradients are a central parameter in much of the analysis presented in this study. The interpretation of surface fronts observed by profiling gliders is not trivial and a number of assumptions were made in the presentation of the results.

In this field campaign, the Seaglider was piloted to complete repeat bow-tie patterns over a single geographical area. A complete bow-tie took, on average, 7 days to complete. Sampling fronts in this way means that the Seaglider may sample a single front multiple times. Given the transient nature of surface submesoscale fronts and a ML eddy growth rate of ~ 10 hours, it is unlikely that the same front is indeed sampled multiple times by the Seaglider. Moreover, the background mean flow was $\sim 8 \text{ cm s}^{-1}$, compared

to the velocity of the Seaglider $\sim 23 \text{ cm s}^{-1}$. Nevertheless, the data is analysed such that the results do not rely on repeat sampling of a front, or the sampling of many fronts, but provides a basis by which to statistically estimate the average presence and strength of these fine-scale fronts and associated impact on the ML, acknowledging that individual features can be very different.

We assume the Seaglider samples fronts perpendicularly. Acknowledging this is not the case, a statistical analysis shows that the lateral gradients are underestimated by a factor of 0.64. Compared to the lateral gradients captured by a Sailbuoy (measuring values of b_x up to $0.06 \text{ kg m}^{-3} \text{ km}^{-1}$, Swart et al., 2020), which was sampling the study site concurrently, the lateral gradients observed by the Seaglider are small (b_x up to $0.015 \text{ kg m}^{-3} \text{ km}^{-1}$), but nevertheless comparable to those observed in the Arctic MIZ by Seagliders ($\sim 0.03 \text{ kg m}^{-3} \text{ km}^{-1}$, Timmermans and Windsor, 2013). Furthermore, using averaged ML lateral gradients also reduces the magnitude of lateral gradients, compared to taking the lateral gradients in the middle of the ML (Thompson et al., 2016).

Additionally, synoptic winds are not always oriented directly downstream or upstream of the fronts. The Seaglider interpretation of the EBF can be analysed by computing the observed EBF (EBF_{obs}) to the actual EBF (EBF_{actual}), estimated from all the observed Seaglider angles and wind angles with respect to a fixed buoyancy gradient (following Thompson et al. (2016)). The Seaglider tends to capture either all or little of the EBF, however this method can also overestimate EBF if the wind stress is aligned perpendicular to the front but interpreted as orthogonal. On average, the ratio of the root mean square of EBF_{obs} to EBF_{actual} is 0.71, suggesting that the EBF values presented here are underestimated.

4.5.2 Regionality

We present the results with reference to Antarctic MIZs, but our conclusions are drawn from a subset of high resolution data within a $1^\circ \times 1^\circ$ degree box at the northern edge of the Weddel Sea MIZ. We focus on the interactions of processes which are likely prevalent throughout the ice-impacted Southern Ocean. However, we acknowledge that the Antarctic MIZ varies regionally in terms atmospheric forcing. For example, the Amundsen Sea Low (ASL) controls winds near West Antarctica. If the zonal winds are intensified because of a deeper ASL, the melt of sea ice occurs earlier in the spring season and

solar warming over summer is enhanced (Holland et al., 2017). In such a case, it is likely that submesoscale processes will be more suppressed during summer. In this way, different regions may experience different leading order forcing mechanisms (like the ASL), which may alter the conclusions drawn from these results.

5 Conclusion

Throughout this study we have demonstrated the influence of sea ice derived fresh water on the vertical and lateral structure of the ML. Predominantly northwards Ekman transport of sea ice meltwater stratifies the ML in the Antarctic MIZ. However, at the same time, the strong north-south mesoscale gradients from the sea ice meltwater creates conditions for the formation of submesoscale MLEs. We show that while these MLEs are confined to the surface boundary layer because of the strong stratification, wind interactions with the resultant fine-scale fronts enhance ML variability. The winds interact with the fine-scale fronts, increasing variability within the ML through both stratifying and destratifying buoyancy fluxes induced by cross-front Ekman driven transport. When the freshwater source decreases later in summer, the magnitude of lateral buoyancy gradients, as well as the submesoscale EBF also decrease. These results show that sea ice impacted MLs, while predominantly forced by the 1D influx of meltwater during summer, cannot be solely treated as 1D systems. Submesoscale fronts are enhanced by the meltwater mesoscale gradients, modulating the influence of winds on the ML. It therefore becomes possible that the ML response to wind forcing and subsequently, heat and freshwater transport, may be misrepresented in coupled-climate models if the submesoscale is not resolved or accurately parameterized.

Acknowledgments

This work was supported by the following grants of SS: Wallenberg Academy Fellowship (WAF 2015.0186), Swedish Research Council (VR 2019-04400), STINT-NRF Mobility Grant. SN and SS: NRF-SANAP (SNA170522231782) and SN, the Young Researchers Establishment Fund (YREF 2019 0000007361). SS and MdP have received funding from the European Union’s Horizon 2020 research and innovation programme under grant agreement No 821001 (SO-CHIC). AFT is supported by ONR (N00014-19-1-2421), NSF (1829969) and a Linde Center Discovery Fund grant. We thank Sea Technology Services (STS), SANAP, the captain and crew of the S.A. Agulhas II for their field-work/ technical assistance.

Zach Erickson, Mar Flexas, and Giuliana Viglione (Caltech) contributed to glider piloting throughout the deployment. S.S. is grateful to Geoff Shilling and Craig Lee (APL, University of Washington) for hosting gliders on IOP. B. Queste is thanked for insightful discussions on glider processing and thermal lag corrections, which was made possible through the UCT-UEA Newton Fund. Special thanks is extended to Isabelle Anson for the generous support of I. Giddy in her doctoral studies and training, from which this paper is derived (SANAP 110733 SAMOC-SA). I. Giddy is further supported by the Oppenheimer Memorial Trust. ERA5 data are generated using Copernicus Climate Change Service Information, available online (www.ecmwf.int/en/forecasts/datasets/archivedatasets/reanalysisdatasets/era5). All the data used for this analysis can be accessed online (<ftp://ssh.roammiz.com>) via anonymous login and navigate to giddy_2020. The code used to produce this analysis is available at <http://doi.org/10.5281/zenodo.4043036>.

References

- Abernathey, R. P., Ceroveck, I., Holland, P. R., Newsom, E., Mazloff, M., & Talley, L. D. (2016). Water-mass transformation by sea ice in the upper branch of the Southern Ocean overturning. *Nature Geoscience*, 9(8), 596–601. Retrieved from <https://doi.org/10.1038/ngeo2749> doi: 10.1038/ngeo2749
- Biddle, L. C., & Swart, S. (2020). The Observed Seasonal Cycle of Submesoscale Processes in the Antarctic Marginal Ice Zone. *Journal of Geophysical Research: Oceans*, 125(6). Retrieved 2020-06-16, from <https://onlinelibrary.wiley.com/doi/abs/10.1029/2019JC015587> doi: 10.1029/2019JC015587
- Bitz, C. M., Gent, P. R., Woodgate, R. A., Holland, M. M., & Lindsay, R. (2006). The Influence of Sea Ice on Ocean Heat Uptake in Response to Increasing CO₂. *Journal of Climate*, 19(11), 2437–2450. Retrieved 2020-06-21, from <https://journals.ametsoc.org/jcli/article/19/11/2437/31163/The-Influence-of-Sea-Ice-on-Ocean-Heat-Uptake-in> doi: 10.1175/JCLI3756.1
- Boccaletti, G., Ferrari, R., & Fox-Kemper, B. (2007). Mixed Layer Instabilities and Restratification. *Journal of Physical Oceanography*, 37(9), 2228–2250. Retrieved from <https://doi.org/10.1175/JPO3101.1> doi: 10.1175/JPO3101.1
- Boutin, J., Vergely, J. L., Marchand, S., D’Amico, F., Hasson, A., Kolodziejczyk, N.,

- 790 ... Vialard, J. (2018). New SMOS Sea Surface Salinity with reduced system-
 791 atic errors and improved variability. *Remote Sensing of Environment*, 214, 115
 792 – 134. Retrieved from [http://www.sciencedirect.com/science/article/
 793 pii/S0034425718302517](http://www.sciencedirect.com/science/article/pii/S0034425718302517) doi: <https://doi.org/10.1016/j.rse.2018.05.022>
- 794 Brenner, S., Rainville, L., Thomson, J., & Lee, C. (2020). The evolution of a shallow
 795 front in the Arctic marginal ice zone. *Elem Sci Anth*, 8(1), 17. Retrieved
 796 2020-06-21, from [https://www.elementascience.org/article/10.1525/
 797 elementa.413/](https://www.elementascience.org/article/10.1525/elementa.413/) doi: 10.1525/elementa.413
- 798 Callies, J., & Ferrari, R. (2018). Baroclinic Instability in the Presence of Convection.
 799 *Journal of Physical Oceanography*, 48(1), 45–60. Retrieved 2020-06-22, from
 800 [https://journals.ametsoc.org/jpo/article/48/1/45/44025/Baroclinic
 801 -Instability-in-the-Presence-of](https://journals.ametsoc.org/jpo/article/48/1/45/44025/Baroclinic-Instability-in-the-Presence-of) doi: 10.1175/JPO-D-17-0028.1
- 802 Callies, J., Ferrari, R., Klymak, J. M., & Gula, J. (2015). Seasonality in subme-
 803 soscale turbulence. *Nature Communications*, 6(1), 6862. Retrieved from
 804 <https://doi.org/10.1038/ncomms7862> doi: 10.1038/ncomms7862
- 805 Charney, J. G. (1971). Geostrophic Turbulence. *Journal of the Atmo-*
 806 *spheric Sciences*, 28(6), 1087–1095. Retrieved from [https://doi
 807 .org/10.1175/1520-0469\(1971\)028<1087:GT>2.0.CO;2](https://doi.org/10.1175/1520-0469(1971)028<1087:GT>2.0.CO;2) (_eprint:
 808 [https://journals.ametsoc.org/jas/article-pdf/28/6/1087/3417468/1520-
 809 0469\(1971\)028-1087-gt-2.0-co-2.pdf](https://journals.ametsoc.org/jas/article-pdf/28/6/1087/3417468/1520-0469(1971)028-1087-gt-2.0-co-2.pdf)) doi: 10.1175/1520-0469(1971)028<1087:
 810 GT>2.0.CO;2
- 811 Chemke, R., & Polvani, L. M. (2020). Using multiple large ensembles to eluci-
 812 date the discrepancy between the 1979-2019 modeled and observed Antarctic
 813 sea-ice trends. *Geophysical Research Letters*. Retrieved 2020-07-30, from
 814 <https://onlinelibrary.wiley.com/doi/abs/10.1029/2020GL088339> doi:
 815 10.1029/2020GL088339
- 816 de Boyer Montégut, C., Madec, G., Fischer, A. S., Lazar, A., & Iudicone, D.
 817 (2004). Mixed layer depth over the global ocean: An examination of
 818 profile data and a profile-based climatology. *Journal of Geophysical Re-*
 819 *search: Oceans*, 109(C12). Retrieved 2020-05-10, from [https://agupubs
 820 .onlinelibrary.wiley.com/doi/abs/10.1029/2004JC002378](https://agupubs.onlinelibrary.wiley.com/doi/abs/10.1029/2004JC002378) (_eprint:
 821 <https://agupubs.onlinelibrary.wiley.com/doi/pdf/10.1029/2004JC002378>) doi:
 822 10.1029/2004JC002378

- 823 Dewey, S. R., Morison, J. H., & Zhang, J. (2017). An Edge-Referenced Sur-
 824 face Fresh Layer in the Beaufort Sea Seasonal Ice Zone. *Journal of Physi-*
 825 *cal Oceanography*, 47(5), 1125–1144. Retrieved 2020-06-21, from [https://](https://journals.ametsoc.org/jpo/article/47/5/1125/44575/An-EdgeReferenced-Surface-Fresh-Layer-in-the)
 826 [journals.ametsoc.org/jpo/article/47/5/1125/44575/An-EdgeReferenced](https://journals.ametsoc.org/jpo/article/47/5/1125/44575/An-EdgeReferenced-Surface-Fresh-Layer-in-the)
 827 [-Surface-Fresh-Layer-in-the](https://journals.ametsoc.org/jpo/article/47/5/1125/44575/An-EdgeReferenced-Surface-Fresh-Layer-in-the) doi: 10.1175/JPO-D-16-0158.1
- 828 du Plessis, M., Swart, S., Ansorge, I. J., Mahadevan, A., & Thompson, A. F.
 829 (2019). Southern Ocean Seasonal Restratisation Delayed by Submesoscale
 830 Wind-Front Interactions. *Journal of Physical Oceanography*, 49(4), 1035–
 831 1053. Retrieved from <https://doi.org/10.1175/JPO-D-18-0136.1> doi:
 832 10.1175/JPO-D-18-0136.1
- 833 D’Asaro, E., Lee, C., Rainville, L., Harcourt, R., & Thomas, L. (2011). Enhanced
 834 Turbulence and Energy Dissipation at Ocean Fronts. *Science*, 332(6027),
 835 318. Retrieved from [http://science.sciencemag.org/content/332/6027/](http://science.sciencemag.org/content/332/6027/318.abstract)
 836 [318.abstract](http://science.sciencemag.org/content/332/6027/318.abstract) doi: 10.1126/science.1201515
- 837 Fox-Kemper, B., Ferrari, R., & Hallberg, R. (2008). Parameterization of Mixed
 838 Layer Eddies. Part I: Theory and Diagnosis. *Journal of Physical Oceanog-*
 839 *raphy*, 38(6), 1145–1165. Retrieved from [https://doi.org/10.1175/](https://doi.org/10.1175/2007JP03792.1)
 840 [2007JP03792.1](https://doi.org/10.1175/2007JP03792.1) doi: 10.1175/2007JPO3792.1
- 841 Frajka-Williams, E., Eriksen, C. C., Rhines, P. B., & Harcourt, R. R. (2011). Deter-
 842 mining Vertical Water Velocities from Seaglider. *Journal of Atmospheric and*
 843 *Oceanic Technology*, 28(12), 1641–1656. Retrieved from [https://doi.org/10](https://doi.org/10.1175/2011JTECH0830.1)
 844 [.1175/2011JTECH0830.1](https://doi.org/10.1175/2011JTECH0830.1) doi: 10.1175/2011JTECH0830.1
- 845 Frölicher, T., Sarmiento, J., Paynter, D., Dunne, J., Krasting, J., & Winton, M.
 846 (2015). Dominance of the Southern Ocean in Anthropogenic Carbon and
 847 Heat Uptake in CMIP5 Models. *Journal of Climate*, 28, 862–886,. doi:
 848 10.1175/JCLI-D-14-00117.1.
- 849 Garau, B., Ruiz, S., Zhang, W. G., Pascual, A., Heslop, E., Kerfoot, J., & Tin-
 850 toré, J. (2011). Thermal Lag Correction on Slocum CTD Glider Data.
 851 *Journal of Atmospheric and Oceanic Technology*, 28(9), 1065–1071. Re-
 852 trieved from <https://doi.org/10.1175/JTECH-D-10-05030.1> doi:
 853 10.1175/JTECH-D-10-05030.1
- 854 Gregor, L., Ryan-Keogh, T. J., Nicholson, S.-A., du Plessis, M., Giddy, I., &
 855 Swart, S. (2019). GliderTools: A Python Toolbox for Processing Under-

- 856 water Glider Data. *Frontiers in Marine Science*, 6, 738. Retrieved from
 857 <https://www.frontiersin.org/article/10.3389/fmars.2019.00738> doi:
 858 10.3389/fmars.2019.00738
- 859 Haumann, F. A., Gruber, N., & Münnich, M. (2020). Sea-Ice Induced Southern
 860 Ocean Subsurface Warming and Surface Cooling in a Warming Climate. *AGU*
 861 *Advances*, 1(2). Retrieved 2020-08-20, from [https://onlinelibrary.wiley](https://onlinelibrary.wiley.com/doi/abs/10.1029/2019AV000132)
 862 [.com/doi/abs/10.1029/2019AV000132](https://onlinelibrary.wiley.com/doi/abs/10.1029/2019AV000132) doi: 10.1029/2019AV000132
- 863 Haumann, F. A., Gruber, N., Münnich, M., Frenger, I., & Kern, S. (2016). Sea-
 864 ice transport driving Southern Ocean salinity and its recent trends. *Nature*,
 865 537(7618), 89–92. Retrieved from <https://doi.org/10.1038/nature19101>
 866 doi: 10.1038/nature19101
- 867 Holland, M. M., Landrum, L., Raphael, M., & Stammerjohn, S. (2017). Spring-
 868 time winds drive Ross Sea ice variability and change in the following au-
 869 tumn. *Nature Communications*, 8(1), 731. Retrieved 2020-06-23, from
 870 <http://www.nature.com/articles/s41467-017-00820-0> doi: 10.1038/
 871 s41467-017-00820-0
- 872 Horvat, C., Tziperman, E., & Campin, J.-M. (2016). Interaction of sea ice floe
 873 size, ocean eddies, and sea ice melting. *Geophysical Research Letters*, 43(15),
 874 8083–8090. Retrieved 2020-06-21, from [http://doi.wiley.com/10.1002/](http://doi.wiley.com/10.1002/2016GL069742)
 875 2016GL069742 doi: 10.1002/2016GL069742
- 876 Kirkman, C. H., & Bitz, C. M. (2011). The Effect of the Sea Ice Freshwater Flux
 877 on Southern Ocean Temperatures in CCSM3: Deep-Ocean Warming and De-
 878 layed Surface Warming. *Journal of Climate*, 24(9), 2224–2237. Retrieved from
 879 <https://doi.org/10.1175/2010JCLI3625.1> doi: 10.1175/2010JCLI3625.1
- 880 Koenig, Z., Fer, I., Kolås, E., Fossum, T. O., Norgren, P., & Ludvigsen, M. (2020).
 881 Observations of Turbulence at a Near-Surface Temperature Front in the Arc-
 882 tic Ocean. *Journal of Geophysical Research: Oceans*, 125(4). Retrieved
 883 2020-06-21, from [https://onlinelibrary.wiley.com/doi/abs/10.1029/](https://onlinelibrary.wiley.com/doi/abs/10.1029/2019JC015526)
 884 2019JC015526 doi: 10.1029/2019JC015526
- 885 Lu, K., Weingartner, T., Danielson, S., Winsor, P., Dobbins, E., Martini, K., &
 886 Statscewich, H. (2015). Lateral mixing across ice meltwater fronts of the
 887 Chukchi Sea shelf. *Geophysical Research Letters*, 42(16), 6754–6761. Retrieved
 888 2020-06-21, from <https://onlinelibrary.wiley.com/doi/abs/10.1002/>

- 2015GL064967 doi: 10.1002/2015GL064967
- Lueck, R. G., & Picklo, J. J. (1990). Thermal Inertia of Conductivity Cells: Observations with a Sea-Bird Cell. *Journal of Atmospheric and Oceanic Technology*, 7(5), 756–768. Retrieved from [https://doi.org/10.1175/1520-0426\(1990\)007<0756:TIOCCO>2.0.CO;2](https://doi.org/10.1175/1520-0426(1990)007<0756:TIOCCO>2.0.CO;2) doi: 10.1175/1520-0426(1990)007<0756:TIOCCO>2.0.CO;2
- Luo, H., Bracco, A., Cardona, Y., & McWilliams, J. C. (2016). Submesoscale circulation in the northern Gulf of Mexico: Surface processes and the impact of the freshwater river input. *Ocean Modelling*, 101, 68 – 82. Retrieved from <http://www.sciencedirect.com/science/article/pii/S1463500316300014> doi: <https://doi.org/10.1016/j.ocemod.2016.03.003>
- Lévy, M., Klein, P., Tréguier, A.-M., Iovino, D., Madec, G., Masson, S., & Taka-hashii, K. (2010). Modifications of gyre circulation by sub-mesoscale physics. *Ocean Modelling*, 34(1-2), 1–15. Retrieved 2020-06-28, from <https://linkinghub.elsevier.com/retrieve/pii/S1463500310000582> doi: 10.1016/j.ocemod.2010.04.001
- Mahadevan, A., D’Asaro, E., Lee, C., & Perry, M. J. (2012). Eddy-Driven Stratification Initiates North Atlantic Spring Phytoplankton Blooms. *Science*, 337(6090), 54–58. Retrieved from <https://science.sciencemag.org/content/337/6090/54> doi: 10.1126/science.1218740
- Manucharyan, G. E., & Thompson, A. F. (2017). Submesoscale Sea Ice-Ocean Interactions in Marginal Ice Zones. *Journal of Geophysical Research: Oceans*, 122(12), 9455–9475. Retrieved from <https://agupubs.onlinelibrary.wiley.com/doi/abs/10.1002/2017JC012895> doi: 10.1002/2017JC012895
- McDougall, T. J., & Barker, P. M. (2011). *Getting started with TEOS-10 and the Gibbs Seawater (GSW) Oceanographic Toolbox*. Battery Point, Tas.: Trevor J McDougall. (OCLC: 724024071)
- McWilliams, J. C. (2016). Submesoscale currents in the ocean. *Proceedings of the Royal Society A: Mathematical, Physical and Engineering Sciences*, 472(2189), 20160117. Retrieved from <https://royalsocietypublishing.org/doi/abs/10.1098/rspa.2016.0117> doi: 10.1098/rspa.2016.0117
- Newman, L., Heil, P., Trebilco, R., Katsumata, K., Constable, A., van Wijk, E., ... Spreen, G. (2019). Delivering Sustained, Coordinated, and Integrated Obser-

- 922 vations of the Southern Ocean for Global Impact. *Frontiers in Marine Science*,
 923 6, 433. Retrieved 2020-08-25, from [https://www.frontiersin.org/article/](https://www.frontiersin.org/article/10.3389/fmars.2019.00433/full)
 924 10.3389/fmars.2019.00433/full doi: 10.3389/fmars.2019.00433
- 925 Parkinson, C. L. (2014). Global Sea Ice Coverage from Satellite Data: An-
 926 nual Cycle and 35-Yr Trends. *Journal of Climate*, 27(24), 9377–9382.
 927 Retrieved from <https://doi.org/10.1175/JCLI-D-14-00605.1> doi:
 928 10.1175/JCLI-D-14-00605.1
- 929 Patoux, J., Yuan, X., & Li, C. (2009). Satellite-based midlatitude cyclone statis-
 930 tics over the Southern Ocean: 1. Scatterometer-derived pressure fields and
 931 storm tracking. *Journal of Geophysical Research: Atmospheres*, 114(D4).
 932 Retrieved from [https://agupubs.onlinelibrary.wiley.com/doi/abs/](https://agupubs.onlinelibrary.wiley.com/doi/abs/10.1029/2008JD010873)
 933 10.1029/2008JD010873 doi: 10.1029/2008JD010873
- 934 Pellichero, V., Sallée, J.-B., Chapman, C. C., & Downes, S. M. (2018). The south-
 935 ern ocean meridional overturning in the sea-ice sector is driven by freshwa-
 936 ter fluxes. *Nature Communications*, 9(1), 1789. Retrieved from [https://](https://doi.org/10.1038/s41467-018-04101-2)
 937 doi.org/10.1038/s41467-018-04101-2 doi: 10.1038/s41467-018-04101-2
- 938 Pellichero, V., Sallée, J.-B., Schmidtko, S., Roquet, F., & Charrassin, J.-B. (2017).
 939 The ocean mixed layer under Southern Ocean sea-ice: Seasonal cycle and forc-
 940 ing. *Journal of Geophysical Research: Oceans*, 122(2), 1608–1633. Retrieved
 941 from [https://agupubs.onlinelibrary.wiley.com/doi/abs/10.1002/](https://agupubs.onlinelibrary.wiley.com/doi/abs/10.1002/2016JC011970)
 942 2016JC011970 doi: 10.1002/2016JC011970
- 943 Richards, K. J., Whitt, D. B., Brett, G., Bryan, F. O., Feloy, K., & Long, M. C.
 944 (2020). *The impact of climate change on ocean submesoscale activity*
 945 (preprint). Oceanography. Retrieved 2020-06-30, from [http://www.essoar](http://www.essoar.org/doi/10.1002/essoar.10503524.1)
 946 .org/doi/10.1002/essoar.10503524.1 doi: 10.1002/essoar.10503524.1
- 947 Rocha, C. B., Chereskin, T. K., Gille, S. T., & Menemenlis, D. (2016). Mesoscale
 948 to Submesoscale Wavenumber Spectra in Drake Passage. *Journal of Phys-
 949 ical Oceanography*, 46(2), 601–620. Retrieved 2020-06-21, from [https://](https://journals.ametsoc.org/jpo/article/46/2/601/12557/Mesoscale-to-Submesoscale-Wavenumber-Spectra-in)
 950 journals.ametsoc.org/jpo/article/46/2/601/12557/Mesoscale-to
 951 -Submesoscale-Wavenumber-Spectra-in doi: 10.1175/JPO-D-15-0087.1
- 952 Rudnick, D. L., & Cole, S. T. (2011). On sampling the ocean using underwa-
 953 ter gliders. *Journal of Geophysical Research: Oceans*, 116(C8). Retrieved
 954 from <https://agupubs.onlinelibrary.wiley.com/doi/abs/10.1029/>

- 2010JC006849 doi: 10.1029/2010JC006849
- Smith, M., Stammerjohn, S., Persson, O., Rainville, L., Liu, G., Perrie, W., ...
Thomson, J. (2018). Episodic Reversal of Autumn Ice Advance Caused
by Release of Ocean Heat in the Beaufort Sea. *Journal of Geophysical Re-*
search: Oceans, 123(5), 3164–3185. Retrieved 2020-06-21, from [http://](http://doi.wiley.com/10.1002/2018JC013764)
doi.wiley.com/10.1002/2018JC013764 doi: 10.1002/2018JC013764
- Speer, K., Rintoul, S. R., & Sloyan, B. (2000). The Diabatic Deacon Cell*. *Jour-*
nal of Physical Oceanography, 30(12), 3212–3222. Retrieved from [https://](https://doi.org/10.1175/1520-0485(2000)030<3212:TDDC>2.0.CO;2)
doi.org/10.1175/1520-0485(2000)030<3212:TDDC>2.0.CO;2 (_eprint:
[https://journals.ametsoc.org/jpo/article-pdf/30/12/3212/4440514/1520-](https://journals.ametsoc.org/jpo/article-pdf/30/12/3212/4440514/1520-0485(2000)030_3212_tddc.2_0_co.2.pdf)
0485(2000)030_3212_tddc.2_0_co.2.pdf) doi: 10.1175/1520-0485(2000)030<3212:
TDDC>2.0.CO;2
- Spreen, G., Kaleschke, L., & Heygster, G. (2008). Sea ice remote sensing using
AMSR-E 89-GHz channels. *Journal of Geophysical Research: Oceans*, 113.
doi: 10.1029/2005JC003384.
- Stone, P. H. (1970). On Non-Geostrophic Baroclinic Stability: Part II. *Jour-*
nal of the Atmospheric Sciences, 27(5), 721–726. Retrieved from [https://doi](https://doi.org/10.1175/1520-0469(1970)027<0721:ONGBSP>2.0.CO;2)
.org/10.1175/1520-0469(1970)027<0721:ONGBSP>2.0.CO;2 doi: 10.1175/
1520-0469(1970)027<0721:ONGBSP>2.0.CO;2
- Swart, S., du Plessis, M. D., Thompson, A. F., Biddle, L. C., Giddy, I., Linders,
T., ... Nicholson, S.-A. (2020). Submesoscale Fronts in the Antarc-
tic Marginal Ice Zone and Their Response to Wind Forcing. *Geophys-*
ical Research Letters, 47(6), e2019GL086649. Retrieved from [https://](https://agupubs.onlinelibrary.wiley.com/doi/abs/10.1029/2019GL086649)
agupubs.onlinelibrary.wiley.com/doi/abs/10.1029/2019GL086649 doi:
10.1029/2019GL086649
- Swart, S., Gille, S. T., Delille, B., Josey, S., Mazloff, M., Newman, L., ... Zappa,
C. J. (2019). Constraining Southern Ocean Air-Sea-Ice Fluxes Through
Enhanced Observations. *Frontiers in Marine Science*, 6, 421. Retrieved
2020-08-25, from [https://www.frontiersin.org/article/10.3389/](https://www.frontiersin.org/article/10.3389/fmars.2019.00421/full)
fmars.2019.00421/full doi: 10.3389/fmars.2019.00421
- Swart, S., Speich, S., Ansorge, I. J., & Lutjeharms, J. R. E. (2010). An altimetry-
based gravest empirical mode south of Africa: 1. Development and vali-
dation. *Journal of Geophysical Research*, 115(C3), C03002. Retrieved

- 2020-06-21, from <http://doi.wiley.com/10.1029/2009JC005299> doi:
10.1029/2009JC005299
- Swart, S., Thomalla, S. J., & Monteiro, P. M. S. (2015). The seasonal cycle of mixed layer dynamics and phytoplankton biomass in the Sub-Antarctic Zone: A high-resolution glider experiment. *Journal of Marine Systems*, 147, 103 – 115. Retrieved from <http://www.sciencedirect.com/science/article/pii/S0924796314001535> doi: <https://doi.org/10.1016/j.jmarsys.2014.06.002>
- Thomas, L. N., & Lee, C. M. (2005). Intensification of Ocean Fronts by Down-Front Winds. *Journal of Physical Oceanography*, 35(6), 1086–1102. Retrieved 2020-05-10, from <http://journals.ametsoc.org/doi/10.1175/JPO2737.1> doi: 10.1175/JPO2737.1
- Thomas, L. N., Tandon, A., & Mahadevan, A. (2013). Submesoscale Processes and Dynamics. In *Ocean Modeling in an Eddying Regime* (pp. 17–38). American Geophysical Union (AGU). Retrieved from <https://agupubs.onlinelibrary.wiley.com/doi/abs/10.1029/177GM04> (eprint: <https://agupubs.onlinelibrary.wiley.com/doi/pdf/10.1029/177GM04>) doi: 10.1029/177GM04
- Thompson, A. F., Lazar, A., Buckingham, C., Naveira Garabato, A. C., Damerell, G. M., & Heywood, K. J. (2016). Open-Ocean Submesoscale Motions: A Full Seasonal Cycle of Mixed Layer Instabilities from Gliders. *Journal of Physical Oceanography*, 46(4), 1285–1307. Retrieved from <https://doi.org/10.1175/JPO-D-15-0170.1> doi: 10.1175/JPO-D-15-0170.1
- Timmermans, M.-L., Cole, S., & Toole, J. (2012). Horizontal Density Structure and Restratification of the Arctic Ocean Surface Layer. *Journal of Physical Oceanography*, 42(4), 659–668. Retrieved 2020-06-21, from <https://journals.ametsoc.org/jpo/article/42/4/659/11336/Horizontal-Density-Structure-and-Restratification> doi: 10.1175/JPO-D-11-0125.1
- Timmermans, M.-L., & Winsor, P. (2013). Scales of horizontal density structure in the Chukchi Sea surface layer. *Continental Shelf Research*, 52, 39 – 45. Retrieved from <http://www.sciencedirect.com/science/article/pii/S0278434312002919> doi: <https://doi.org/10.1016/j.csr.2012.10.015>
- Turner, J. (1973). *Buoyancy effects in Fluids*. Cambridge: Cambridge University Press.

- 1021 Vichi, M., Eayrs, C., Alberello, A., Bekker, A., Bennetts, L., Holland, D., ... Tofo-
 1022 foli, A. (2019). Effects of an Explosive Polar Cyclone Crossing the Antarc-
 1023 tic Marginal Ice Zone. *Geophysical Research Letters*, 46(11), 5948–5958.
 1024 Retrieved from [https://agupubs.onlinelibrary.wiley.com/doi/abs/](https://agupubs.onlinelibrary.wiley.com/doi/abs/10.1029/2019GL082457)
 1025 10.1029/2019GL082457 doi: 10.1029/2019GL082457
- 1026 Viglione, G. A., Thompson, A. F., Flexas, M. M., Sprintall, J., & Swart, S. (2018).
 1027 Abrupt Transitions in Submesoscale Structure in Southern Drake Passage:
 1028 Glider Observations and Model Results. *Journal of Physical Oceanog-*
 1029 *raphy*, 48(9), 2011–2027. Retrieved from [https://doi.org/10.1175/](https://doi.org/10.1175/JPO-D-17-0192.1)
 1030 JPO-D-17-0192.1 doi: 10.1175/JPO-D-17-0192.1
- 1031 von Appen, W.-J., Wekerle, C., Hehemann, L., Schourup-Kristensen, V., Konrad,
 1032 C., & Iversen, M. H. (2018). Observations of a Submesoscale Cyclonic Fil-
 1033 ament in the Marginal Ice Zone. *Geophysical Research Letters*. Retrieved
 1034 2020-06-21, from <http://doi.wiley.com/10.1029/2018GL077897> doi:
 1035 10.1029/2018GL077897